

# Laser-assisted fabrication of tissue engineering scaffolds from titanium alloys

26

*I.V. Shishkovsky*<sup>1,2</sup>

<sup>1</sup>Lebedev Physics Institute (LPI) of Russian Academy of Sciences, Samara, Russia; <sup>2</sup>Moscow State Technological University named "STANKIN", Moscow, Russia

## 26.1 Introduction

Several millions of reparative operations for replacing bone tissue with metallic implants and endoprostheses are performed every year. These operations are typical for maxillofacial surgery, neurosurgery, traumatology, orthopedy, and stomatology. The main property required for an implant is reliability; it must be able to function as a bone tissue substitute over a long period of time. The reliability is affected most of all by the possibility of osteointegration, the durable ingrowth of an implant into a bone without inflammatory reactions, which facilitates implant rejection. The implant should be made of a biocompatible material, possess sufficient durability, and have a large surface area in contact with the bone.

Of the metals used for implants, about 50% are titanium and its alloys. These are optimal materials for implants in terms of their biocompatibility and strength-to-weight ratio. Their comparatively low usage is due to the low manufacturability of titanium, and, consequently, the expense of the implants, prepared mainly by mechanical treatment. Further, final polishing of the surfaces in contact with the bone is quite complex. There are basically no cast implants, although titanium alloy molding is widely applied in the aerospace industry. This is because pure titanium has low casting properties and its castable alloys contain components like nickel or vanadium, which have a detrimental influence on the tissues around the implant. In order to increase the application of titanium in medicine, special durable alloys and new implant constructions and technologies for designing them are needed.

Tens of firms around the world are engaged in the design and production of implants and endoprostheses. Most of the recognized constructions are fixed to bones by their external surface. To increase the contact surface, the implants are applied using macroretence systems like incisions and incavations or deposited with special coverings. The helical implants used in stomatology have their surface treated in order to obtain the special microrelief that increases the contact surface. Recently, porous implants have been manufactured by casting cobalt-chrome alloys or sintering titanium grains. The most complete (and most expensive) endoprostheses have a porous surface composed of a layer of spatial multiradial "stars." The porous implant is fixed to a bone by its external surface, due to the tissue invasion into the pores. However,

the porous surfaces of the implants are not regular because the cells differ in size and monolithic zones can occur. The tissue invading the pores is not always sufficiently supplied, which can lead to osteoporosis and other complications. All the implant systems are unified; this means that all the implants being manufactured vary in size but are similar in form. This seriously constrains the use of implantation in complicated cases.

In neurosurgery and maxillofacial surgery, titanium implants in the form of perforated plates are used. The position of the plates is adjusted during the operation. This prolongs the operation (and the time under anaesthetic for the patient), leads to deformation of the mounting holes and, above all, to the occurrence of stress concentration zones, which lowers the durability of the implant.

The results of many research studies [1,2] show the many possibilities of applying an intermetallic nickel-titanium NiTi, which has the useful property of shape memory even in the porous form, as a biocompatible material for medical implants. This substance is promising for orthopaedy as well as manufacturing of prosthetic elements capable of self-righting, self-fixing, and self-functioning at physiological temperature.

The traditional methods of obtaining this material have an essential disadvantage, which is the laboriousness of fabricating functional medical implants with individual predetermined size and shape.

The idea of using rapid prototyping (RP) technology and the selective laser sintering (SLS) method in medicine is common [3–14]. But the problem at issue is how to synthesize the models of the implants' forms or the implants themselves from powder materials such as titanium, its alloys (Ti-Al-V), and stainless steel. The next logical step for practical implantology has been made. It consists of the direct SLS of intermetallic phase NiTi in a controlled laser influence (LI) space [15]. This way of fabricating medical implants with their individual form predetermined by three-dimensional computer modelling is quite promising. At the same time, the initial powder of NiTi can be saturated with hydroxyapatite to increase the biocompatibility of the implants [2]. Biosimulating additives can also be infiltrated to accelerate the process of implantation.

The abstract mentioned [16] some factors to consider for the better use of implants: (a) the bone quality in patients over 60 is lowered; (b) the majority of high-strength materials for prostheses have higher modules of elasticity compared to bone tissue, so stress concentration zones can appear; and (c) micromotion on the implant-bone interface leads to the instability of that interface, the deterioration of the implant, and damage to the bone. The transitional zone between the implant and the bone is therefore of great importance and should have an optimal macro-, micro-, and probably nanostructure as well as a strong linkage.

Gaggl *et al.* [17] demonstrated in their research that the interfacial durability between the implant and a bone essentially increases when using a rough surface at the place of contact. This guarantees reliable growth of the tissue into the pores and durable mechanical bonding between the implant and the substrate [18]. Also the topography of the contact surface should be adjusted to the real structure of the bone. Different types of bones in the human body have different structures, making it quite difficult to ensure the durability of the implant and bone join with ingrowth of the tissue only. Consequently, it is essential to search for some methods that allow

the use of alternative ways of fixing to the bone surface, taking into account the individual structural characteristics of different people. The gradient porosity structure can be realized through the SLS method [2,15]. A shielding medium prevents oxidation of the nitinol particles in the sintering process, although in some studies titanium oxide is seen as a favorable phase [16,19].

Nitinol powders (NiTi phase >99.7 wt.%) of P55H45 grade and titanium powders (Ti >98.1 wt.%) of PTOM grade were purchased at the Polema Company (Tula, Russia). Prior to laser sintering, the powders were dried in a vacuum oven for 2 h at 300 °C. The particle size of all starting powders was ~100 µm (in order to be commensurate with the diameter of the laser spot) and was checked using a sieve analysis.

The SLS requires sensitive selective treatment of the powder composition for layer-by-layer synthesis of the premodelled implants. Choosing the laser beam (LB) parameters, including power density, scanning velocity, and focusing spot diameter and its overlap coefficient, is therefore of fundamental importance.

The RP process via the SLS of biomatrices involves the following steps [2,20] (Figure 26.1):

- Preparation of a computer-aid design (CAD) of a future scaffold.
- Program-based fabrication of the transversal sections of a 3-D object.
- Layer-by-layer superposition of these sections during the laser additive process.

The CAD stage (Figure 26.1, stage I) is conducted in the framework of CAD-CAE packages such as *Solid Work* (Dassault Systems), or *Pro-Engineering* (Parametric Technology), or the specialized package *Mimic* (Materialize) used in medical tomography treatment. Such packages have utilities for modelling the internal porous structure, including a gradient of some biophysical properties (porosity, permeability,

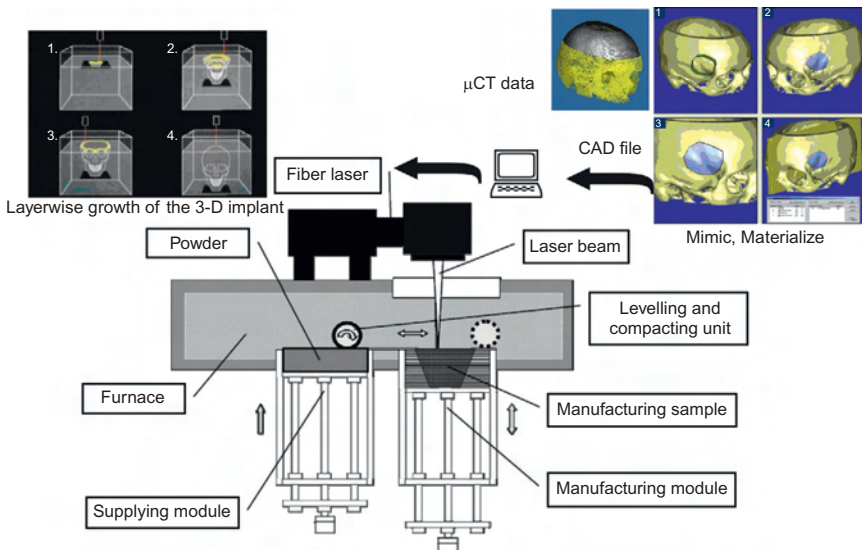


**Figure 26.1** Schematic diagram of the SLS setup by 3-D data of tomography.

element concentration, etc.). The program divides the image into sections to render it in its actual size later on.

The SLS machine (Figure 26.1, stage II) consists of a table with two containers attached to it. The bottom of each container is a piston. Initially, one of the containers (the left one) is filled with the powder while the other is left empty with its piston placed at table level. The agglomeration can be carried out in an argon or nitrogen medium at low or high temperature. The untapped powder in one of the containers “supports” the implant during its formation while the powder from the other container can be recycled.

Provided that the laser power is high, the sintering process is transformed into the melting one. Thus a solid, practically cast 3-D part (implant) can be created that is very important for bone reconstruction.

In the photo in Figure 26.2, samples of the synthesized 3-D parts are shown: a pure titanium plate for maxillofacial surgery (a), a molar of nickel titanium (b) and a layered 3-D titanium cladding on a stomatological dowel (c).

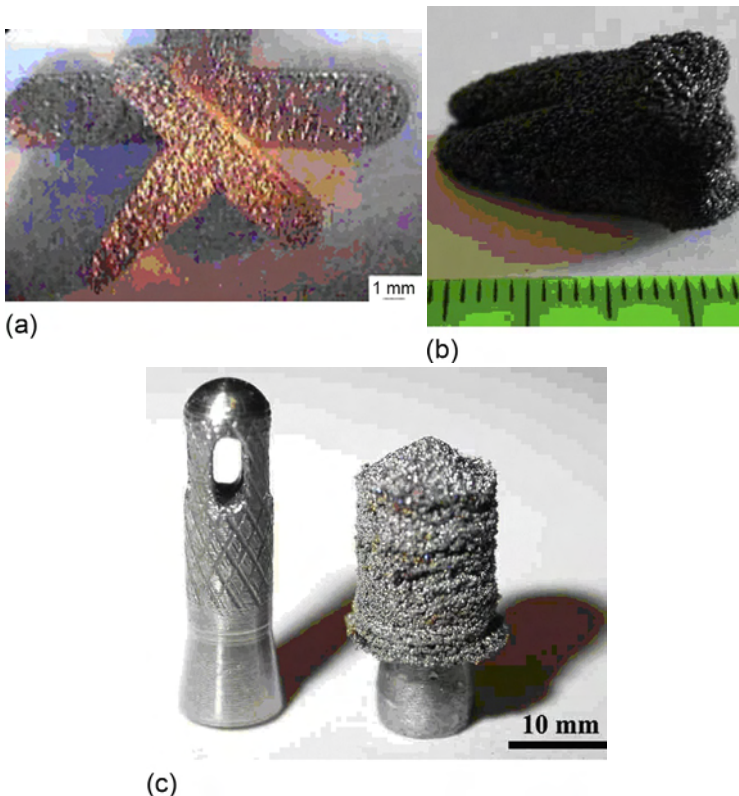


**Figure 26.2** (a–c) 3-D parts for use in stomatology.

Using the SLS method can reduce the period of fabrication of the prosthetic parts by accelerating the stages of designing, modelling, and adjustment. It will also reduce the cost of the suggested technology in comparison with traditional methods. Material resources are also saved because cheaper domestically produced powders are used. At the same time, the new properties and functional characteristics of the biocompatible titanium and nickel titanium implants and their influence on the cost of prosthetics in the fields of their application (sports medicine, stomatology, orthopaedy) are yet to be valued.

## **26.2 Influence of the selective laser sintering (SLS)-technique-obtained 3-D porous matrix for tissue engineering on the culture of multipotent mesenchymal stem cells**

In traumatology, maxillofacial surgery, and stomatology, the application of implants is very important for various pathologies. The quality and biological compatibility of the implant material and its structure influence the efficiency of the implant applications [21]. At present, most of the implant producers are testing their products on animals. However it cannot be assumed that these results can be extrapolated directly to human beings [22]. Besides, it should be noted that the use of animals for such experiments is not ethical, especially now that alternative techniques are available. Implant testing on cellular cultures is commonly used as the first stage of biological testing for biocompatibility and toxicity of implants [23].

Multipotent mesenchymal stromal stem cells (MMSC) are a promising autologous material for cell therapy and tissue engineering because they can be found inside almost any conjunctive tissue [24]. Active participation of the MMSC in the regeneration processes has been proven by many authors [25]. MMSC usage allows one to show the properties of the implant material on the cell level. This provides the opportunity to study the biological properties of implants, such as cytodifferentiation induction, stimulation and suppression of proliferation and migration, and mutagenic and toxic effects of implants. Provided that there are not toxic effects, it is possible to estimate the adhesion properties, velocity and depth of the growth of stem cells in the implant, and hence to conjecture the degree of integrity of the tissue with the implant material [26]. The MMSC approach allows us to gather information about the implant biological properties prior to animal testing, and thus to improve and change the material properties until the desired ones are achieved.

Today tissue scaffold engineering is a widely developed line of the regenerative medicine that covers *in vivo* cultivation of stem cells, fabrication and restoration of damaged or lost tissue, control and testing systems, biological studies and the synthesis of new pharmaceutical products [5,27]. Within this concept, the main interest is building (or stimulating the synthesis) of tissue and organs *in vivo* due to stem cell implantation of the extracellular matrix. In contrast to the conventional method of cell culturing *in vitro*, tissue-engineering scaffolds can be designed so that the shape

strictly meets the individual peculiarities of each patient. A scaffold will not only ensure a support function but also determine the direction of stem cell growth into the extracellular matrix. The matrix structure and contents promote the artificial differentiation of cell and tissue regeneration. This sophisticated approach to tissue synthesis *in vivo* matches their natural development *in situ* [28,29].

In regenerative surgery, it is currently important to replace cast implant materials by porous 3-D matrices having the shape of the body (bone) to be replaced to restore the defective areas. It is generally known that the topography of a porous surface in comparison with a smooth one has an impact on the morphological behavior of cells while stem cell proliferation is influenced by the synergistic action of micron and submicron scale topography [2,30]. A further problem is that the stem cell matrix must have bioptic properties over the whole porous structure where the stem cell mass and newly formed tissue become ingrown during their evolution.

The investigation of regeneration mechanisms for tissues and organs is a relatively new research field. Research into new technologies, which could restore a lost function of an organ or a system, has led to the application of RP and manufacturing technology (RPMT) in biotechnology, tissue engineering, regenerative implant medicine, and organogenesis. These are all based on the transplantation of stem cells into carrier matrices.

A carrier matrix is a synthetic or biological complex with sufficient mechanical strength to act as a support. It is normally made from a porous layered construction. It can be synthesized via the SLS technique using the CAD file for each individual layer by referring to 3-D tomography data. After synthesis of the porous scaffold, the stem cells are adopted inside (i.e., penetrate into) the matrix. The following basic criteria for building a biologically compatible matrix for use in tissue-engineering constructions have been established through experiments: prevention of cytotoxicity; maintenance of adhesion; fixation; proliferation and differentiation of the cells located on its surface; prevention of inflammatory reaction on the material surface and immune response; and sufficient mechanical strength and bioresorption by normal metabolic routes [31,32].

Adult bone tissue is practically incapable of regeneration. As a result of disturbing factors, its defects gradually lead to deterioration or even loss of mobility. Current technologies for prosthetic repair allow complete rehabilitation. However, progress in modern organotypic regenerative medicine encourages research into technologies for bone replacement using natural transplants.

New technologies of bone building using tissue engineering have been developed in several directions. The following process has been called osteogenesis. The cellular mass, consisting of the osteoblasts and human MSSCs, is slurried and jointly cultivated. Biodegradable polymers based on organic acids (polyetheretherketone, polycaprolactone,  $\epsilon$ -caprolactone/hydroxyapatite, PGA, PGLA), traditionally used as matrices, are then formed into three-dimensional implants [33–35]. The cellular mass culture is placed inside the matrix, and, during preparation, transplanted into

the alveolar socket. Here, because of the cellular and tissue properties of the microenvironment, osteogenesis takes place [34].

The present study outlines the results of research into the stem cell adhesion, morphology, and proliferation. It looks at differentiation of porous 3-D tissue-engineering matrices of NiTi synthesized by the SLS process with the aid of dynamic SEM optical microscopy. Comparative morphological analysis of stem cell growth was also carried out in Ref. [2]. All of the titanium graded PTOM and nitinol graded PV N55 T45 powders were obtained from the Russian chemical market and used as supplied. Mixtures of Ti or nitinol with hydroxyapatite (graded HA:GAP-85d) were prepared in order to increase the implant biocompatibility. As a result of LB sintering, flat monolayers were used for morphological analysis ( $10 \times 30 \times d$  mm, where  $d$  is the depth of monolayer).

According to a technique developed previously [20], the external appearance of the porous matrix of NiTi proper and NiTi with HA additives was modelled via CAD-CAE and synthesized by previously determined LI methods. Figure 26.3 shows a common scheme for the medical experiment and the configuration of the nitinol scaffolds.

Morphological analysis was carried out in collaboration with CRL SamSMU (Prof. Volova L.T.) for Case Study 1 and with the Cell Technologies Centre of Samara Ministry of Health (Ph.D. Volchkov S.E.) for Case Study 2. In Case Study 1, the experiments were conducted on the primary cultures of dermal fibroblasts and human MMSCs of 4-18 passages. The dermal fibroblast culture was taken from the musculocutaneous tissue within a 6-10 week period using the method of primary explants.

The cells were cultured in standard conditions (thermostat Sanyo, Incubator MIR-262) at  $37^\circ\text{C}$  in the MEM growth medium with 10% embryo beef serum in plastic culture vials (Orange Scientific; Corning) with  $2500\text{ mm}^2$  surface area. The testing process was conducted inside cultured Petri dishes (Sarstedt) with internal

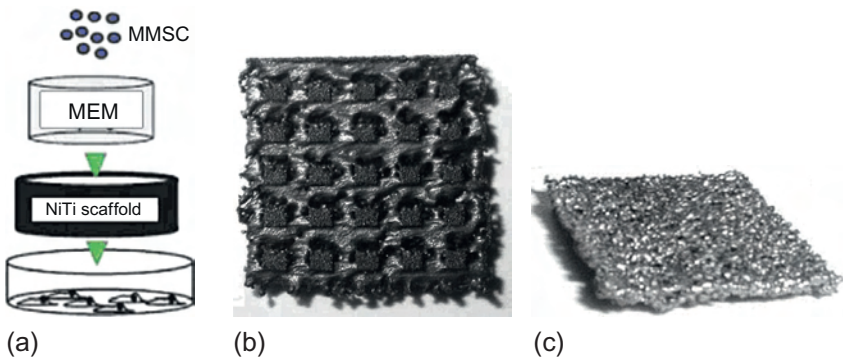


**Figure 26.3** Experiment scheme: (a) configuration of porous NiTi scaffolds with regular (b) and tessellation (c) structures (size of squares were  $10 \times 10\text{ mm}^2$ ).

diameter 30 mm. Experiments were carried out by the direct contact method with two variants, as explained below:

1. Fibroblasts were reseeded from the culture vial onto the Petri dish and then cultured for 24 h. Over this time cellular monolayers with a density of about 315 cells/mm<sup>2</sup> were fabricated. The implants to be studied were inserted into the monolayers.
2. Fibroblasts were reseeded and the implant was inserted simultaneously in the Petri dish. The cell dose was constant in all cases at 200 cells/mm<sup>2</sup>.

The following control parameters were used:

1. Petri dishes with culture growth medium and implants with fibroblasts were not reseeded.
2. Petri dishes with fibroblast culture were passivated and observed simultaneously with experimental samples, but without any supplementary treatment.

Native cultures were studied by using an inverted microscope, called “Biolam P-2-1,” with magnifications of 100× and 150×. Daily visual examination and morphometry of the native culture were undertaken. Cell consistency in each individual monolayer was estimated visually and the desquamation was determined numerically. Size, shape, and cytotoxicity effects were also observed. Usually, in the normal primary culture the fibroblasts had an elongated form, 2-4 appendices, homogeneous cytoplasm, and clear boundaries. The nucleus was generally situated eccentrically and 1-3 nuclei were kept (see [Figure 26.4](#)). After reseeding, the culture medium was checked for common protein content. It was then controlled using a microbiuretic method involving estimation of the free and protein bound oxyproline. Statistical processing was estimated using both parametric and nonparametric tests.

The MMSC were received from the *Wharton's Jelly* of the umbilical cord of newborns (with the authorization of the mother). Stem cells were singled out by the explant method. The materials under consideration were washed with the sterile

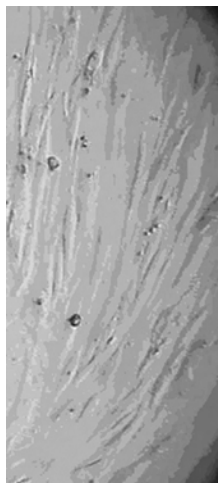


**Figure 26.4** Primary culture of dermal fibroblasts, native culture.

phosphate salt buffer, and then sterilized in the autoclave at a temperature under 121 °C over 30 min.

Two groups were included in the study:

1. Reference or control group, containing only MMSC.
2. NiTi (10 samples for statistics), see [Figure 26.3](#).

The culturing process in the three groups lasted for 26 days under standard cultivation conditions (37 °C, 5% CO<sub>2</sub> in MCO-20AIC (Sanyo) incubator). The nutrient medium comprised  $\mu$ MEM (Sigma) with the following additives: 10% FBS (Gibco), 2 mM L-alanyl-glutamine (Invitrogen). This was changed either every 5 days, or at the moment when the medium indication altered.

We used studies recommended by the international community involved in stem cell therapy to verify that the obtained cells belonged to the MMSC [36]. Immunophenotyping was carried out using these antigens: CD90, CD44, CD106, CD45, HLA-ABC, HLA-DR, 73, 34, 144, 105, 117, 62L, 133, 14, on a continuous-flow cytofluorometer (Becton Dickinson). The induction of cytodifferentiation in osteogenic, chondrogenic, and adipogenic directions was conducted in the following commercially available media: NH Osteodiff, NH Chondrodif, and NH Adipodiff (Miltenyi Biotec) according to the producer's recommendations. The cytodifferentiation was estimated by measuring the stem cell morphology change and the reaction to the specific staining agents (also according to the producer's recommendations). OilRed O (Sigma) was used for the adipogenous estimation, alkaline phosphatase FAST BCIP/NBT (Sigma) for the osteogenesis evaluation, and aggrecan (Abcam) for testing the antibodies. The proliferation activity was estimated with a cellular analyzer of concentration and viability, ViCell XR (Beckman Coulter). The proliferation activity was determined by the equation:

$$X = [\log_{10}(\text{NH}) - \log_{10}(\text{NI})] / \log_{10}(2)$$

where NI is the inoculum cell number, NH is the cell harvest number and  $X$  is the amount of doubling that occurs during each cultivation time.

In order to determine the toxicity of the material, the cellular morphology and morphometry were studied and the velocity of duplication was calculated. The migration ability of stem cells (mechanotaxis) was determined using a time-lapse experiment with the aid of the AxioObserver A1 microscope (Carl Zeiss) with an incubation system. The time-lapse method involves filming MMSC cultivation for 4 h at a video-filming rate of 10 frames per min. The migration ability (mechanotaxis) was evaluated by the comparative method, in which the trajectories of the cell motion between the reference and nitinol groups were compared. The assessment of the video, calculation of the cell migration distance, and morphological analysis were supported by the *Image-Pro PLUS 6.0* (Media Cybernetics) and *AxioVision 4.8* (Carl Zeiss) software. Cluster analysis, which shows a display of moving objects (cells) and calculates their trajectories and distances, was carried out with the bundled software *ImageJ* and *Image Pro Plus*. From this software, division of the cells into groups was estimated according to the density of pixels per object.

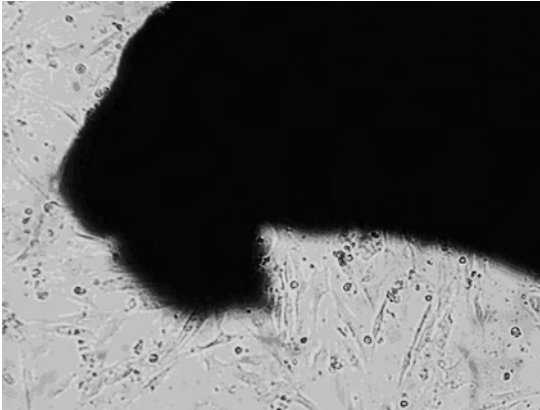


**Figure 26.5** Titanium sample (black) on the fibroblast monolayer (first variant, first day of experiment). Fusiform cells with central nuclei grow in the manner of “scythes” parallel to each other without adhesion. Native culture. Inverting optical microscope (OM). 100 × .

## 26.2.1 First series of experiments

### 26.2.1.1 SLS of titanium powder, first variant

After one day the monolayer density was measured in the regions around the porous implant and was shown to have reduced its coverage by  $136 \text{ cell/mm}^2$ . This was probably a consequence of damage because of sample mobility in the culture solution. The percentage of damaged cells in each individual monolayer was up to 10.2%. The majority of the fibroblasts kept all the characteristics of normal cells. The form and size of cells were not changed, their cytoplasm was homogeneous, and their nuclei were of the light bubble-type with 1-2 nuclei (Figure 26.5).

The monolayer on the bottom surface of the dish was integral and uniform; fibroblasts kept their normal structure, forms, and sizes. Monolayer shape and cell structure were not notably different from normal during all four days of observations. The percentage of damaged cells was about 5-10%. No morphological signs of the implant influencing the fibroblast culture were observed. The cells formed a uniform monolayer. Its density corresponded to the process of culture growth after passivation and was also dependent on distance. The nature and direction of the cell growth for those in close proximity to the sample were constant.

### 26.2.1.2 SLS of titanium powder, second variant

Observation after one day showed that the fibroblasts had adhered to the bottom of the culture dish near the implant edges. The cell body was located around and under the objects being studied (Figure 26.6a and c). The sample itself was on the bottom of the Petri dish. In the detached zone, the fibroblasts produced an incomplete monolayer. The fibroblasts had clearly incorporated into and penetrated the implant.

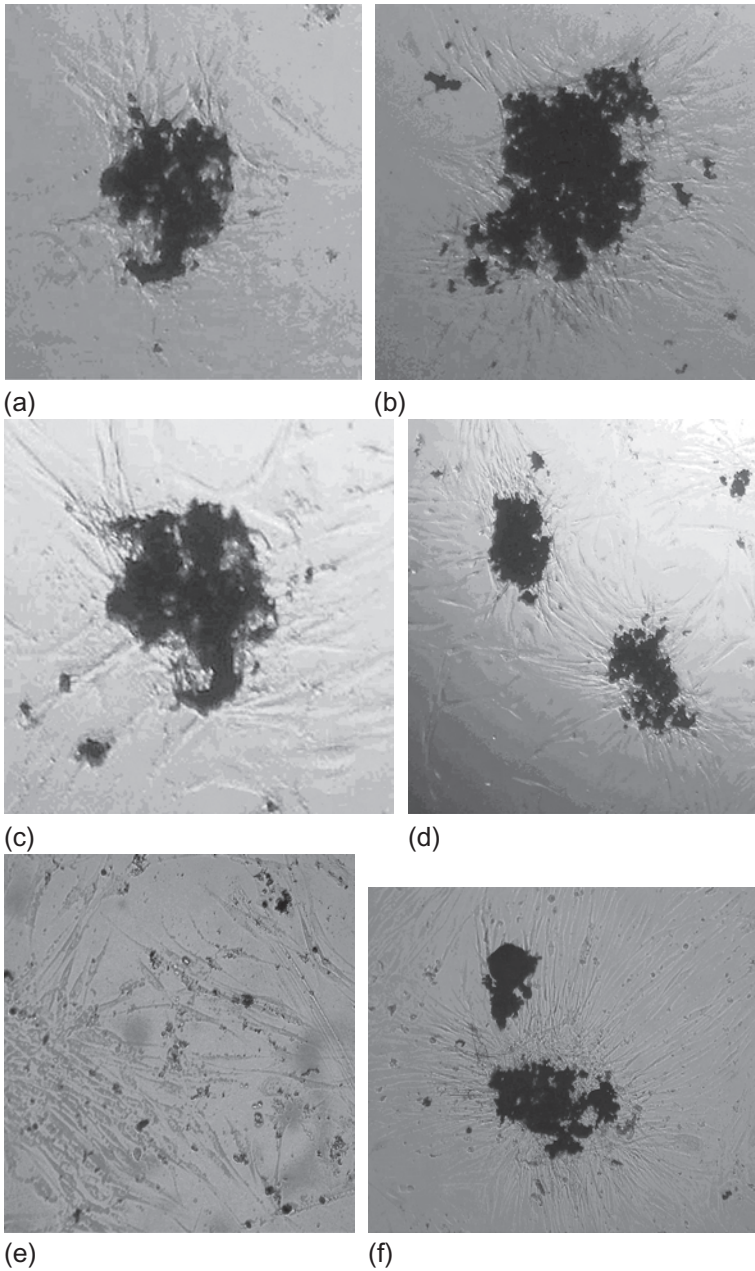


**Figure 26.6** Titanium (a, c, e, g) and nitinol (b, d, f, h) samples on the fibroblastmonolayer (second variant of experiments). Native culture. Inverting OM  $\times 100$ . Scales point out in [Figure 26.7](#).

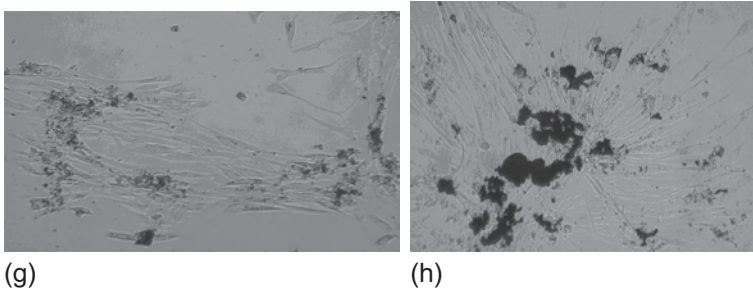


**Figure 26.6** Continued.

These experimental results showed that fibroblasts in the culture demonstrated vastly greater affinity for the very small edges of the porous titanium structure. The process of fibroblast growth (formation of the distinctive “scythes”) occurs in the pore direction and leads to texture formation (Figure 26.6c). Cell density on the surface around these pores quickly increased (Figure 26.6e and f) and by the fourth day of the experiment had achieved saturation density. Fibroblast colonies penetrated into the titanium pores and diffused into its highly porous structure.

After day one of the experiment, near the low-porosity region of the implant, the fibroblast monolayer was noticeably rarer. The cell density had begun to increase and by day four some uniform structure had formed in the regions around the samples. However, these structures had still not reached saturation density. Cells were not located along the edges of the titanium implants.

## 26.2.2 *Second series of experiments*

### 26.2.2.1 *SLS of the nitinol powder, first variant*

After the first day, a reduction of the monolayer density was observed on the whole surface of the culture dish caused by the implant mobility at the bottom of the Petri dish. During the three subsequent days the view of the monolayer was perfected; the monolayer density increased; and the structure, shape, and size of its cells were not distinguishable from normal.

### 26.2.2.2 *SLS of the nitinol powder, second variant*

Under the influence of the testing material, the cells were fixed to the bottom of the culture dish. As a result, the monolayer density had decreased significantly after one day. There was a greater local focus of mass reproduction, where the cells tended to be normal (Figure 26.6b). This focus was much greater than that of the titanium experiments (Figure 26.6a and b). Throughout the observations the fibroblasts had a distinctive morphology, velocity, and growth pattern (Figure 26.6d, f, and h).

### **26.2.3 Third series of experiments**

#### **26.2.3.1 SLS of the titanium powder + HA, first variant**

After one day, a reduction of the monolayer density was observed in cells placed on the culture dish. On the fourth and final day of the experiment the bottom surface of the dish was not distinguishable from normal. The monolayer was homogeneous and fibroblasts kept their usual structure, forms, and sizes.

#### **26.2.3.2 SLS of the titanium powder + HA, second variant**

A significant reduction in the speed of the monolayer growth was observed after 24 h. The cells were mainly concentrated around the small implant pores. On the fourth day of the experiment the cells had practically died. It seems that this is because, in the presence of HA, the reproduction conditions were so favorable that cells had used up the whole nutrient solution and perished.

### **26.2.4 Fourth series of experiments**

#### **26.2.4.1 SLS of the nitinol powder + HA, first variant**

Under the influence of combined intermetallic and hydroxyapatite, the cells were fixed to the bottom of the culture dish very weakly. This meant that after one day the monolayer density was considerably lower than in the control sample. At this point, the cells were attached to the whole area of the bottom of the dish without showing any affinity to the sample. Throughout the observation the fibroblasts kept a distinctive morphology, velocity, and growth.

#### **26.2.4.2 SLS of the nitinol powder + HA, second variant**

Observation over 24 h showed that the fibroblasts were concentrated mainly around the small implant pores. In other areas, the fibroblasts formed a thin monolayer. The shape, size, and fibroblast location in the culture dish were similar to the results of previous observations.

During the investigation of the *in vitro* cultivation process, it was established that initially so-called round cells dominated. After 4 days they were transformed into different cell lines. The dominant population had the fibroblast elements in all the cells. After that, separate processes occurred, including distinct fixing to the dish walls and to the titanium or nitinol samples. This resulted in different cell lines merging and forming the cell monolayers inside the pores. Under cultivation *in vivo*, it was shown that stable chondrogenic and osteogenous elements grew inside the titanium and nitinol pores. Osteoblast colonies in the porous nitinol were formed corresponding to chondro- or bone matrix.

The initial results of Case Study 2 are shown in [Figure 26.7a and b](#). The cells of the reference group proliferated actively compared with this same process nearby the implant edge, which was minimal.

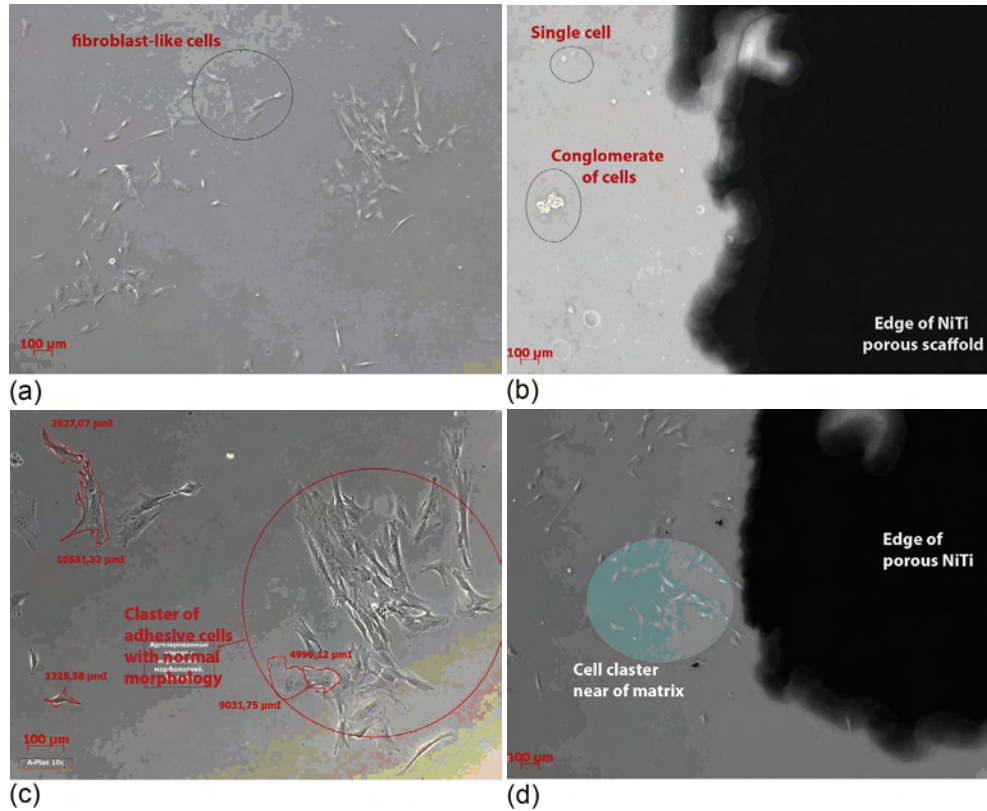


**Figure 26.7** OM images of the start (a, b) and the second day (c, d) of the experiment: (a, c) for the reference group and (b, d) for the edge of the NiTi sample.

By the next day, there was full adhesion of 90% of cells to the Petri dishes in the reference group. The majority of the cells had a typical fibroblast-like (spindle-shaped) shape and a clearly visible nucleus with two or four nucleoli (Figure 26.7a). The increase of the cell population near the NiTi sample edge was less remarkable (Figure 26.7d).

After a week of experiments, the reference group's cellular mass had increased smoothly during the process of cultivation. Culture density increased from 35% to 100% in 10 days of cultivation.

In the NiTi groups (Figure 26.8b), for 10 days the culture density grew substantially slower than the reference group and nonuniformly between the samples in this group (from 75% up to 95%). On the tenth day, maximum densities were registered for group 1 (95%), group 3 (85%), and group 4 (60%). In addition, small colonies were observed in immediate proximity to the material, with the morphological image that suggested "aging" cells. On the material, the first signs of the stem cells were noticed (Figure 26.8c).

These colonies can be seen more clearly in Figure 26.9, after the cellular study had been completed. There is a thin layer of cells visible in the porous 3-D matrix structure.

Hence, in the reference group the formation of a cellular monolayer lasted for 16 days, the proliferation speed was 0.03 and doubled each hour or 0.694 and doubled each day, and the total number of doublings within the period of cultivation was 11.11 (Figure 26.10). A cellular morphology was normal during the whole cultivation process. The natural emergence of "aging" cells in the culture didn't exceed 20% of the whole population. The aging processes were characterized by the increase of cytoplasm and nucleus volume, a growing cell area, cell shape changing into cubic, cellular arrest, and close death (Figure 26.9, vide supra).

At the nitinol group, the proliferation speed was 0.02 doubling per hour or 0.532 doubling per day, and the total number of reduplications within the cultivation period was 10.69. An insignificant effect of proliferation oppression was mentioned as a result of the research in the NiTi series. This was probably related to the heightened porosity of the material.

Depending on the intensity of the stem cell population growth, the analysis and separate samplings of cells were carried out at different stages of the maturing process that characterize the cells' aging according to their morphological characteristics (Figure 26.11). In Figure 26.11 (from right to left and bottom-up) the cells are shown separated by their "age," beginning with the youngest.

A morphological assessment of the pictures was carried out for each group and experiment series on the 3rd, 15th (Figure 26.11), and 25th day of the culturing process. The cells were then sorted into three groups (Table 26.1, Figures 26.11 and 26.12):

- "Immature" (red) cells: these are young, actively dividing cells, spindle-shaped, with an area not exceeding  $5000 \mu\text{m}^2$ . These cells are actively participating in fission and migration.
- "Adult" (blue) cells: these have a triangular or irregular form, with areas ranging from  $5000$  to  $16,000 \mu\text{m}^2$ . These cells are also taking part in proliferation and migration but are much slower.
- "Giant" (yellow-green) cells: these have an irregular shape, sharpened edges, and an enormous surface area ranging from  $16,000$  to  $40,000 \mu\text{m}^2$  and, occasionally, even higher. They are not involved in the division process and are not practically migrating.

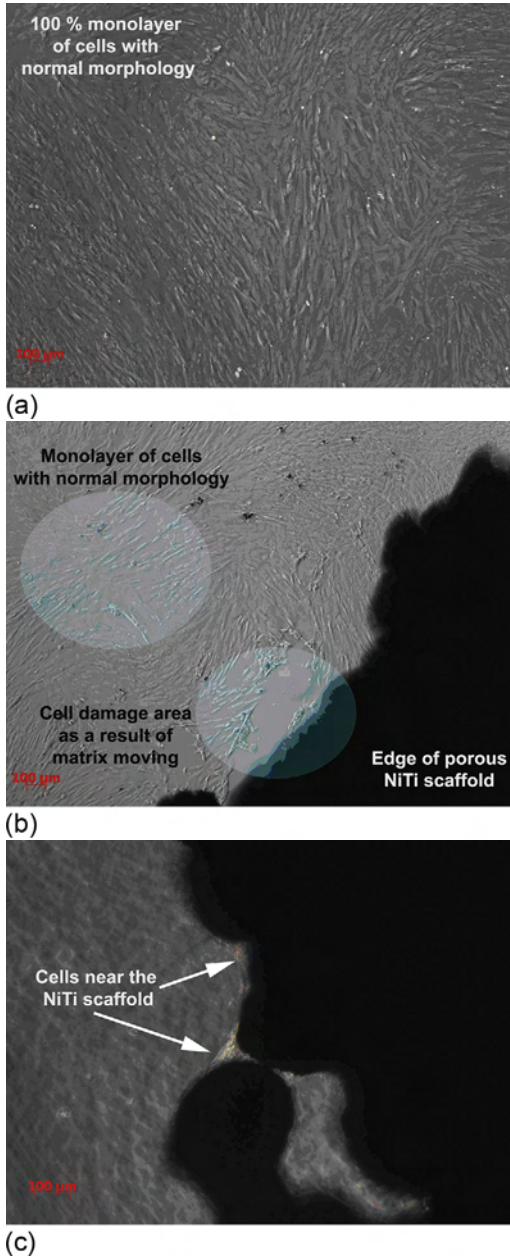


**Figure 26.8** OM images after the week of experiments (a, b): (a) the reference group; (b) the border of the NiTi matrix; and (c) the cell culture near the matrix on the 13th day.

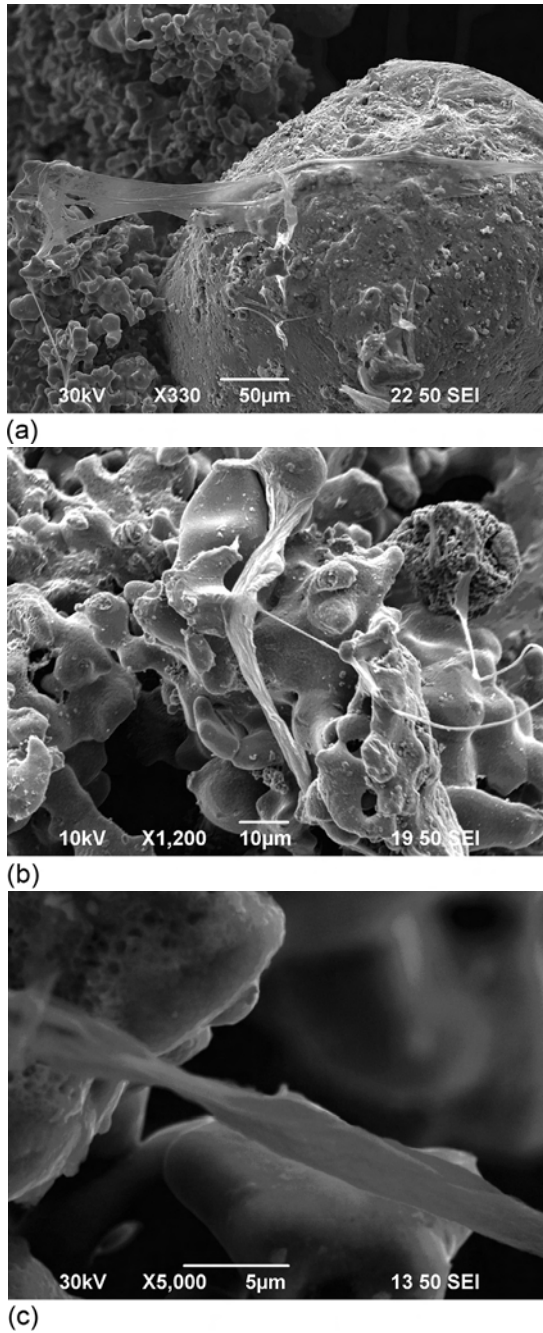


**Figure 26.9** (a–c) Scanning electron microscope investigation of the porous NiTi matrices.

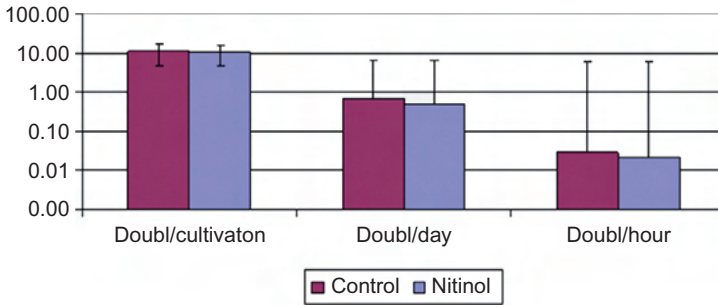


**Figure 26.10** Logarithmic speed of proliferative activity. Root-mean-square difference from the average is shown by vertical lines.



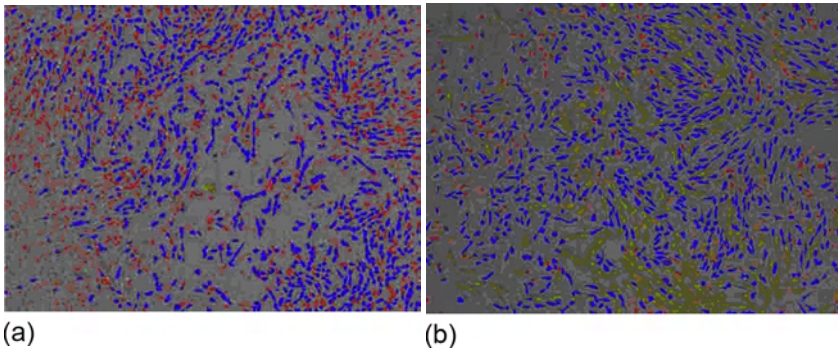
**Figure 26.11** Number and configuration of MMSC colonies.

**Table 26.1 Morphological groups ratio**

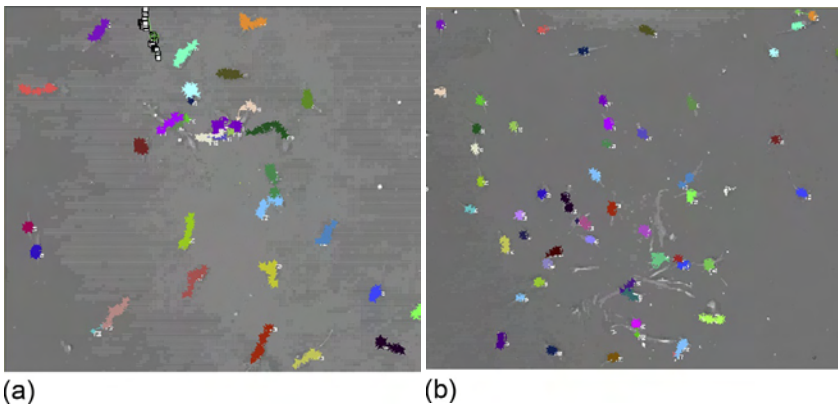
No. of a group	Reference group	NiTi	Reference group	NiTi
	Quantity of objects/% ratio of objects		Aver. area/standard deviation (square/pixel)	
1 group (red)	1797/60.57	1154/65.27	201.5/60.8	174.0/53.8
2 group (blue)	1169/39.41	547/30.94	543.4/210.6	426.6/111.1
3 group (green)	1/0.034	67/3.79	2708.5/0.1	1143.7/482.7

Figure 26.12 shows that the reference group of “young” and actively propagating cells is dominant but, near the 3-D NiTi matrix, the reverse is the case. In the latter, there is a high population of “aging giant” and slow-moving cells. This is why the proliferation velocity in the near-matrix zone is much lower than that in the reference group.

The migration ability (mechanotaxis) was evaluated by comparing the trajectories of the cells motion between the reference and nitinol groups (Figure 26.13 and Table 26.2). During the observation, the average distance covered by the cells in the reference group was ~350 μm, while in the NiTi group the cells covered an average ~42 μm under similar conditions.



**Figure 26.12** Cluster analysis of the stem cells population (“young” cells—red color, “adult” cells—blue color, and “aging” cells—green color): (a) reference group cells and (b) cells in near-scaffold zones.



**Figure 26.13** Motion path and calculation of the distance passed by cells. Duration is 4 h. Magnification of image is 50 $\times$ : (a) reference group and (b) near-matrix zone.

**Table 26.2 Migration activity**

Group	Cells per analysis	Distance ( $\mu\text{m}$ )	Minimum ( $\mu\text{m}$ )	Maximum ( $\mu\text{m}$ )	St. deviation ( $\mu\text{m}$ )
Reference NiTi	34	350.4238	78.70689	768.6559	187.0104
	56	42.494089	8.173793	153.891548	29.881101

The experiments on the cell migration ability revealed that in the reference group, over 4 h, the average distance covered by the stem cells was 350.42  $\mu\text{m}$  (minimum 78.70, maximum 768.65, standard deviation 187.01), as shown in [Table 26.2](#). The stem cell in the near-nitinol zone, under similar conditions, covered an average 42.49  $\mu\text{m}$  (minimum 8.17, maximum 153.89, standard deviation 29.88).

The immunophenotypic study showed that the stability of the testing cells was due to the MMSC group and the absence of the hemopoietic transformation or changes in the linear origin. The testing cells contained the following antigens: CD 90, CD44, HLA-ABC, 73, 105. These are characteristic of stromal cells. The absence of the antigens CD 45, CD106, CD34, CD144, 62L, HLA-DR, 133, 14, confirmed the presence of the MMSC group. In the course of the experiment, the weak positive expression of the marker CD 117 (C-kit) was revealed. This is a receptor for the stem cell factor of stem cell growth. The positive expression of this factor makes it possible to assume that the cells were immature.

As seen in [Section 26.1](#), we have discovered that porosity alone is not enough to grow cells into an implant. The size of the pores is also very important and should be commensurable with the size of the cells (compare [Figures 26.7d](#) and [26.8b](#)). The cells were pulled transversely to the matrix and their density was higher near certain pores, as mentioned in Ref. [29]. Excessive submicron porosity is probably as unfavorable for stem cells of  $\sim 50\text{--}100\ \mu\text{m}$  as its complete lack.

The study presents comparative results of morphological analysis of stem cell growth on porous matrices created by SLS on titanium and nitinol for tissue engineering. It is clear that the creation of tissue scaffolds (for example, for oral and maxillo-facial surgery) is relevant and promising [37]. In particular, it is possible that:

1. The SLS method allows layer-by-layer synthesis of biocompatible implants from pure titanium or nitinol powders, which do not possess measured cytotoxicity. Cell adhesion in the presence of such implants has demonstrated good monolayer conditions in and near the sample area with high cell density. Stem cells retained their structure and proliferative activity.
2. Implants made from Ti, NiTi, Ti+HA and NiTi+HA have high porosity, which provides the possibility for germination and adhesion, although their hardness is problematic.
3. Both options for stem cell proliferation are characterized by high chemotaxis of the cells to the samples, which decreases the number of cells in intermediate areas.
4. The presence of hydroxyapatite does not significantly influence the cell reproduction, indicating the high biocompatibility of titanium and nitinol. The nature of cell growth suggests that titanium is a biotolerant material for implantation, while nitinol is a biocompatible material.
5. The results of the proliferative activity and dynamic differentiation of the MMSC on the SLS-obtained porous Ni-Ti scaffold have been shown. According to the morphometry data, backed up by the SEM, the first MMSC colonies in the NiTi pores were registered on the tenth day. The proliferation speed was 0.694 doubling per day and 0.532 doubling per day for the reference group and the NiTi group, respectively.
6. Another fundamental result still requires explanation. While the percentage of small, but actively proliferating, “young” cells is comparatively high (50%) in the reference group (without scaffold), the stem cells grow up to an enormous size (which is aging) and their proliferation activity slows significantly after bringing in the matrix (the exogenous irritant).

The damaging effect of fibroblasts on the first day of experiments and the inadequate mechanical strength of porous scaffolds mean that they cannot be recommended as a universal material for substrate matrices. Despite these drawbacks, these materials can compete with organotypic polymers. In the future, laser sintering should be adapted for layer-by-layer fusion of such implants, which will allow their use in the replacement of skin, cartilage, and bone defects in surgical practices.

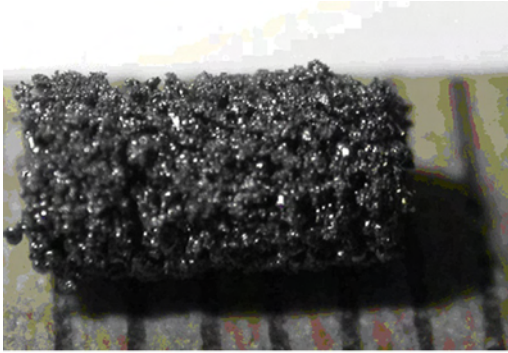
It is important that the issue of supplying the stem cells remains unsolved in the case of using porous Ni and NiTi as a stem cell repository. In the synthesis of bone by the SLS method, the question of blood supply after grafting is not clear either. The technology of direct osteogenesis can cause several problems connected with the creation of a certain tissue microenvironment for the developing bone over 30-35 weeks. Equally, one must admit that the creation of an organ *de novo* will be a major breakthrough for reconstructive orthopaedy.

### **26.3 Preclinical testing of SLS-obtained titan and nitinol implants' biocompatibility and biointegration**

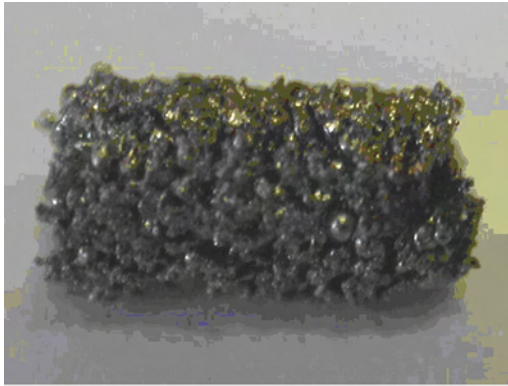
Preclinical research on biointegration of porous nitinol implants compared with that of porous and cast titanium was carried out on a group of 21 laboratory rats over a three-month period at SamSMU (Prof. Volova T.V., M.D. Fokeev S.V.) [38]. All the porous nitinol implants were obtained by the SLS method. The animals were divided into three groups. Implants made of porous sintered nitinol were implanted in the first group, implants of porous titanium in the second one, and the third was the reference group with implants of pure titanium "Rema," as used in stomatology. The appearance of the implants is represented in [Figure 26.14](#).

The area for surgery was prepared using standard techniques with all the common rules regarding asepsis and antiseptics ([Figure 26.15](#)). The insertion site within the bone was formed using a hollow dental burr. The wound was repaired with sutures and treated with iodine solution. Primary intention healing was typical for the wound. Material extraction was carried out after 1, 2, and 3 days and at 1, 2, and 3 months. In all cases the implant remained in a steady position inside the shoulder blade. The color of the implants did not change, possibly indicating a lack of material corrosion. The extracted material was then submerged in formalin solution for four days. After that the specimens were embedded with paraffin and stained with hematoxylin and eosin.

Seven days after implantation, macroscopic analysis showed no signs of edema in the operation area. After the implant extraction in the osteal tissue, a cylindrical defect was observed. From investigation, using optical microscopy, of the tissue specimens of the scapulas, it was established that spongiform osteal tissue was present transformed into trabecules and lacunas. Between the trabecules there was reticular tissue with blood vessels. At the same sites, intensive bone formation was detected by observing the young osteal and reticulofibrous tissue. There were no signs of inflammation. The histological picture for the porous nitinol implants was similar to that of



(a)



(b)



(c)

**Figure 26.14** Appearance of the porous implants of nitinol (a), and titanium (b), synthesized by the layer-by-layer SLS method, and cast titanium (c—spiral) “Rema”.

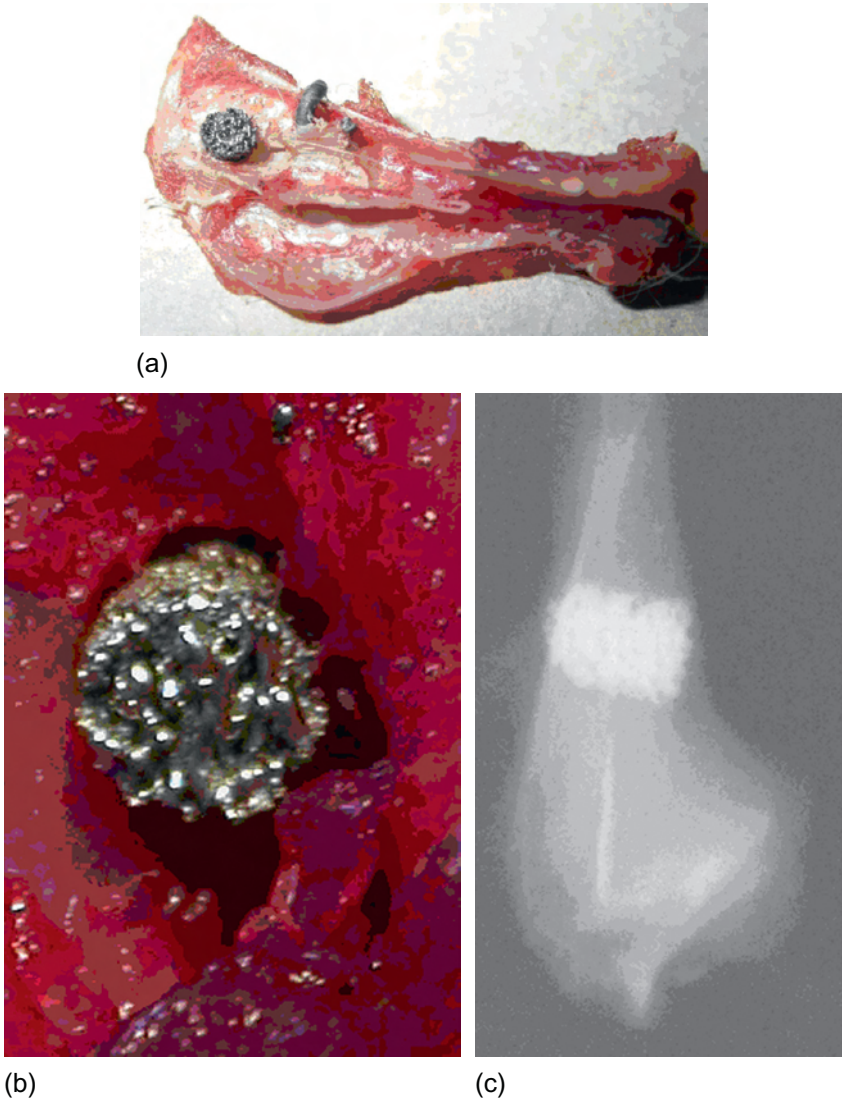
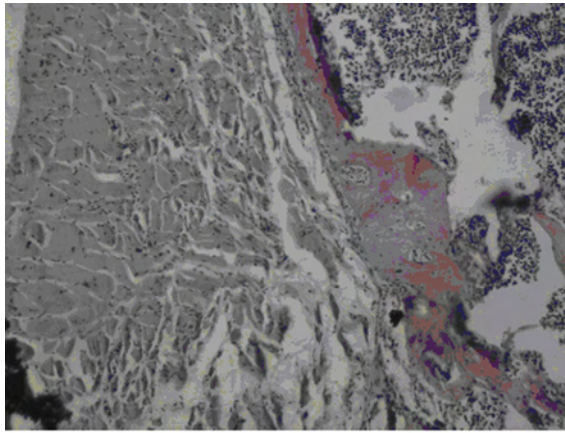


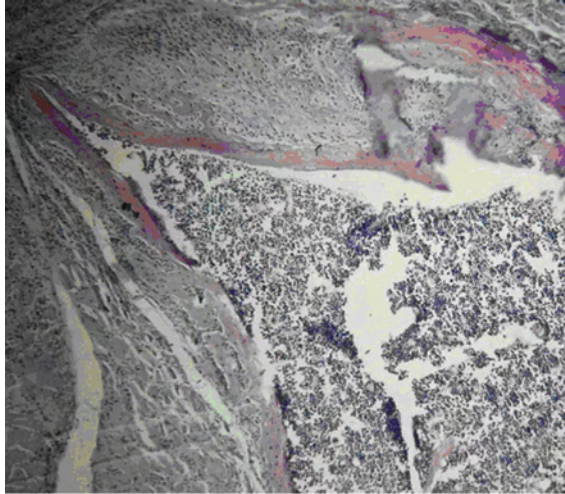
**Figure 26.15** Scapula with the porous implant in it (a), the process of implantation (b), roentgenogram of the implant topography *in vivo* (c—axial view).

the experiments with porous titanium implants (compare [Figures 26.16](#) and [26.17](#) after 1 week and after 2 months). This suggests both of the materials could be used in implantology.

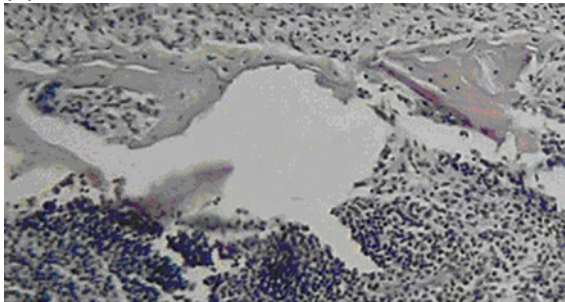
Microscopic analysis of the bone tissue near the titanium spiral revealed the presence of huge cells with 2-3 large nuclei. Among the connective tissue cells, macrophages, fibroblasts, lymphocytes, and plasmocytes were discernible. Reticulofibrous tissue



(a)

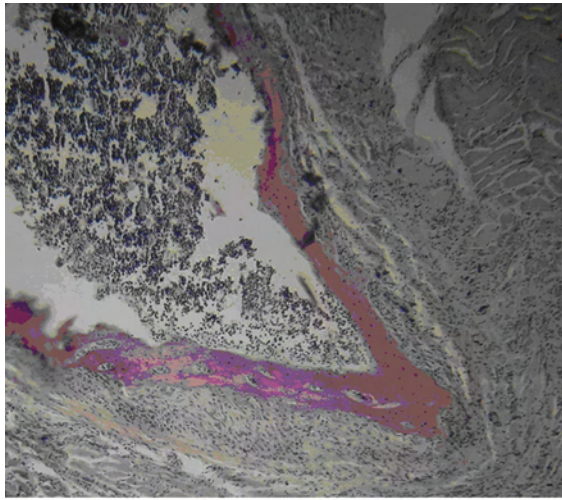


(b)

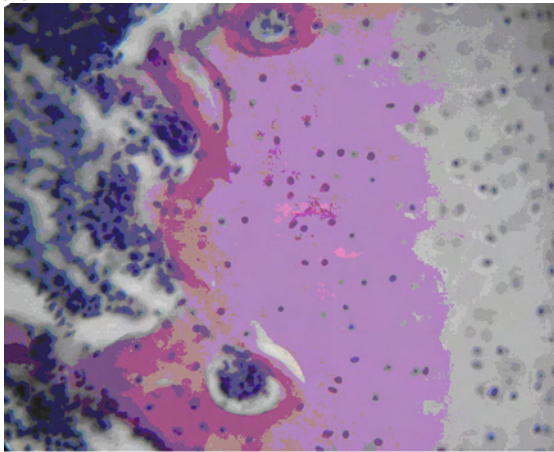


(c)

**Figure 26.16** Periosteal tissue structures after implantation, 1 week. OM, magnification  $40 \times 10$ : (a) porous titanium; (b) porous nitinol; and (c) cast titanium spiral.



(a)

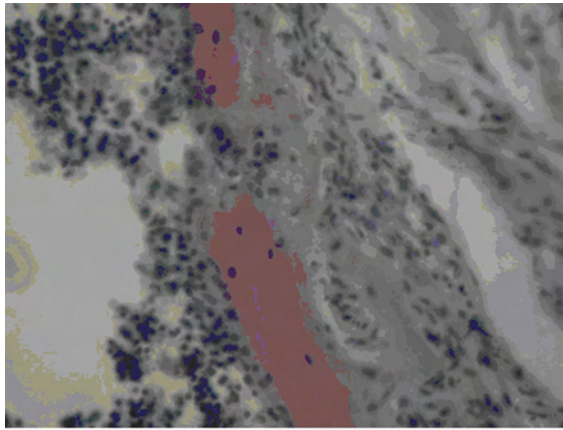


(b)

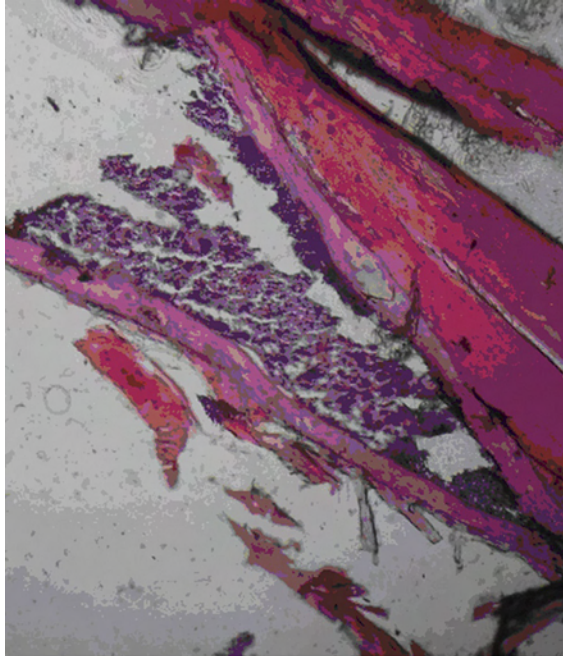
**Figure 26.17** Osseous tissue mount after implantation, 2 months. OM, magnification  $40 \times 10$ : (a) porous titanium and (b) porous nitinol.

accretion toward the muscular tissue was observed in the periosteal area. Histological analysis revealed an osteoplastic process accompanied by the growth of young osteal beams on the edge of the defect (Figure 26.16c).

In the later weeks and months (Figure 26.18), the osteoblasts and osteocytes in the scapula's structures actively rejuvenated. In the connective tissue, randomly located fascicles of collagenic fibers dividing cellular elements were visible. Fibroblasts, macrophages, and lymphocytes were found between the osteal beams as well. A white color (Figure 26.18) showed the formation of fatty tissue. The osteal beams had



(a)

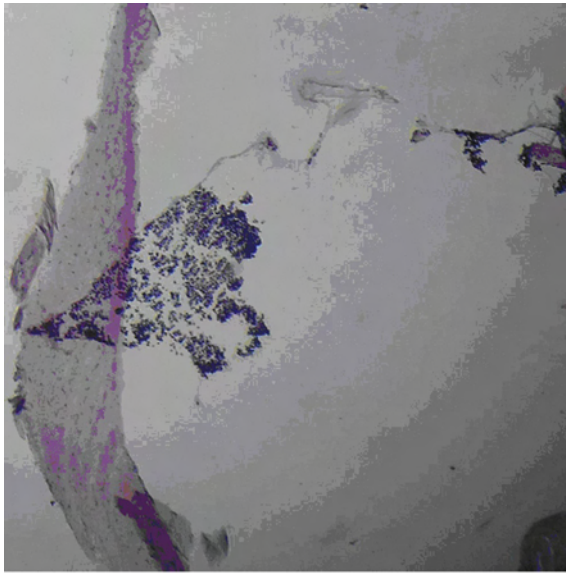


(b)

**Figure 26.18** Periosteal tissue structures after implantation, 3 months. OM, magnification  $40 \times 10$ : (a) porous titanium; (b) porous nitinol; and (c) cast titanium spiral.

the organotypical structure of young spongy bone tissue with lacunas. The lacunas were filled with actively proliferating cells of red bone marrow reticular tissue.

A morphological study of the implant structure, once it had been contained in living tissue, was carried out after the histological study at the SEM (LEO EVO-50 XVP + INCA). [Figure 26.19](#) shows an example of effective penetration of the connective



(c)

**Figure 26.18** Continued.

tissue between the darker granular materials consisting of titanium particles without any signs of necrosis.

Figure 26.19a shows an organotypic structure of the young tissue with lacunae between two large (150–200  $\mu\text{m}$ ) titanium globules. Elemental analysis (EDX—S3, Figure 26.19b) showed the presence of titanium 18.35%, nickel 21.88%, and carbon 59.77%. The nickel to titanium ratio affected the stoichiometry of NiTi intermetallic phase, and the higher quantity of carbon indicated the presence of conjunctive cartilaginous tissue. White areas in Figure 26.19 were caused by fluorescence from electron-beam excited organic structures during SEM.

Figure 26.20 shows clearly that the young conjunctive tissue has grown into a gap between two big particles of titanium. The element analysis (EDX—S3, Figure 26.19b) showed, apart from titanium, the presence of carbon, oxygen, and phosphorus, which are constituents of connective cartilaginous tissue.

Nitinol was completely osseointegrated after three months of biointegration in organotypic structures (Figure 26.21a). Bone/nitinol contacts were close, indicating good tissue tolerance. The implant has a regular open structure (Figure 26.21a), which facilitates the bony tissue ingrowth into the body of the implant resulting in the desirable firm fixation to the bone. Free nickel (Figure 26.21e) was not observed on the nitinol surface, which is important because of its potential toxicity. The presence of calcium in the element composition was due to the decalcination process before the histological study and showed that there was good bone formation. Dark areas

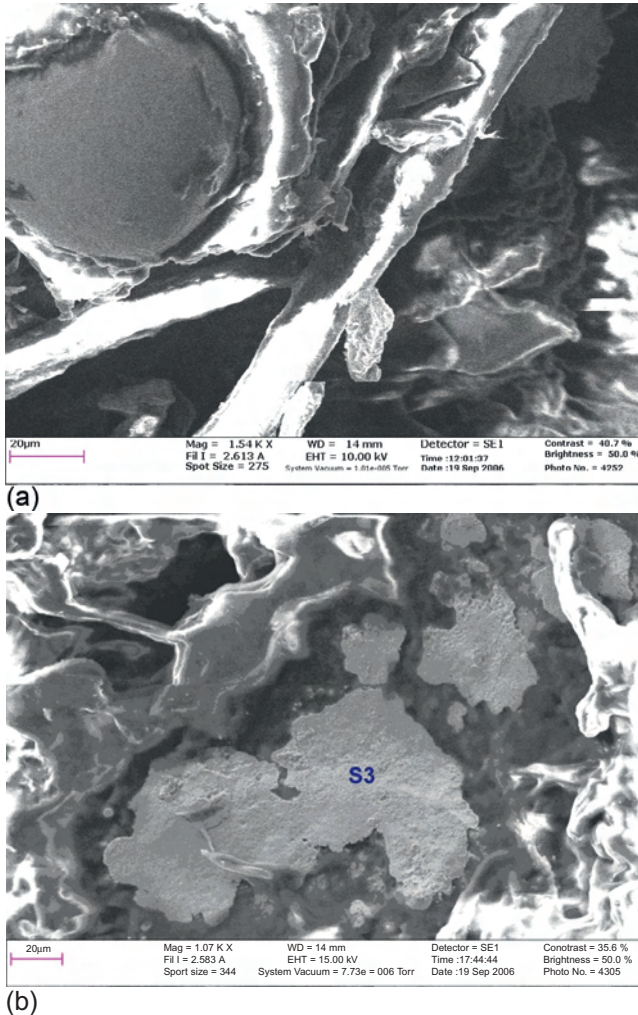


**Figure 26.19** The titanium implant after 3 months: (a) SEM microstructure, magnification 1530 $\times$ , accelerating potential of 10.00 (kV) and (b) the nitinol implant after 3 months. SEM microstructure, magnification: 1070 $\times$ , accelerating potential 15.00 (kV).

in Figures 26.20a, 26.21a, and 26.22a (see S2 in Table 26.3) correspond to carbon inclusions covered with titanium or nitinol particles.

A slight bone resorption could be seen under a microscope at the contact area of the implants. This bone resorption activity was caused by removal of the bone tissue with the dentist's burr during the implant operations. The defect zone kept the organotypic structure. Neutrophilic exudate was not found in any series of probes.

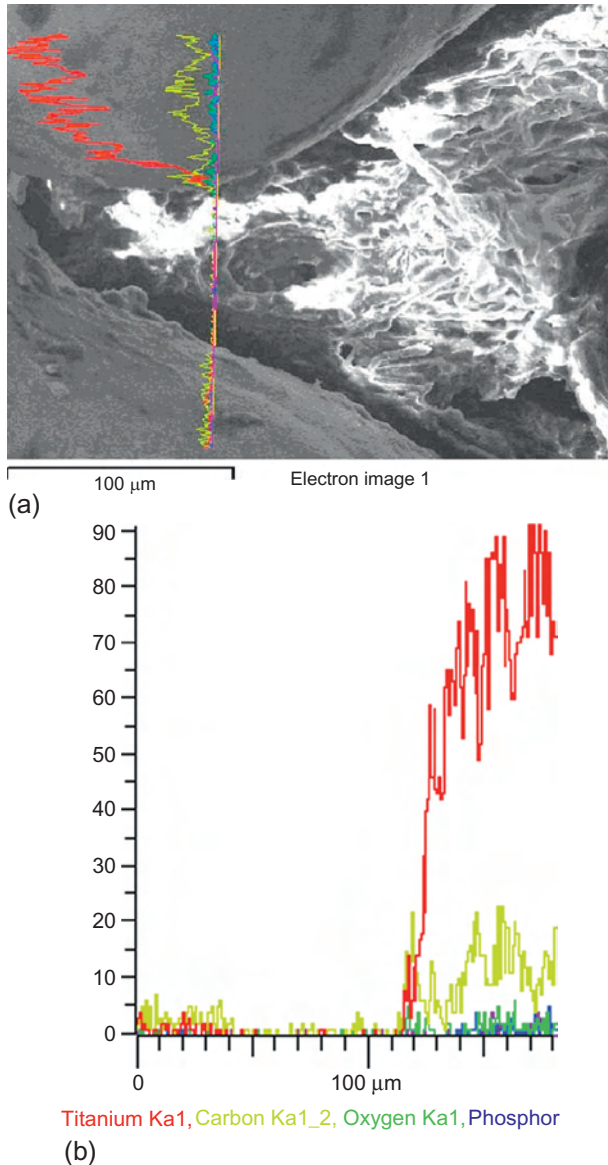
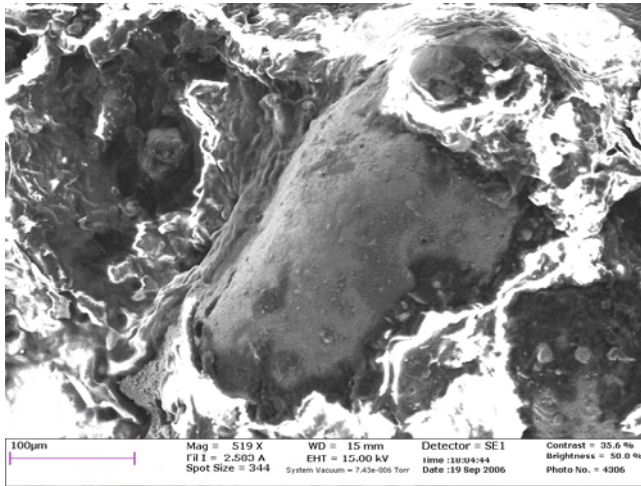
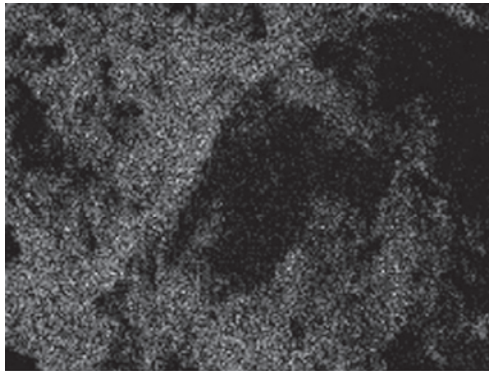


**Figure 26.20** Titanium implant after 3 months: (a) microstructure at magnification of 1186 $\times$ , accelerating potential of 15.00 (kV) and (b) elements' distribution.

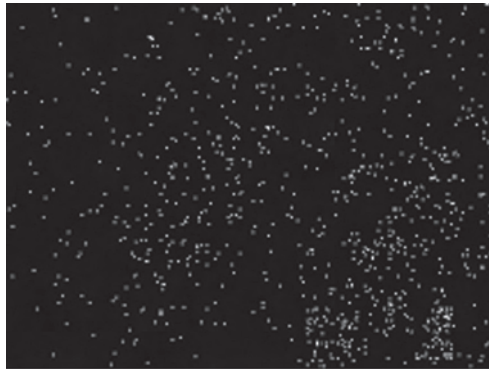
Once the observations had been completed, porous nitinol and titanium implants were closely embedded in the living tissue and were difficult to extract. The osteal tissue surrounding the defect zone had an organotypical structure. The periosteum did not change in thickness, which was slightly different from normal values, and consisted of a cellular and a fibrous layer. Histological analysis showed that the



(a)

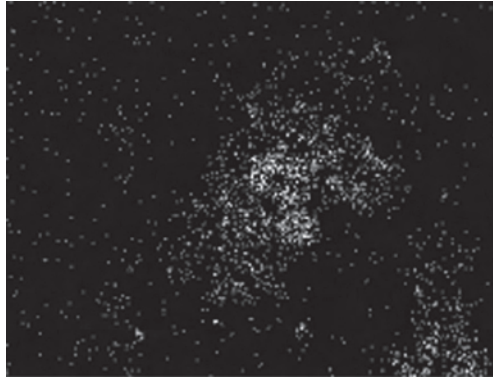


(b) O Ka1\_2



(c) O Ka1

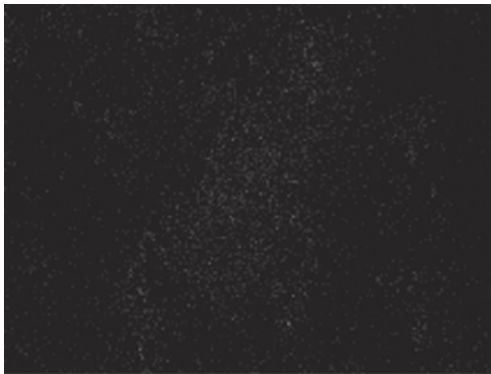
**Figure 26.21** Nitinol implant, 3 months after implantation. (a) Microstructure, magnification: 519 $\times$ , acceleration potential 15.00 (kV) and (b-f) elemental structure.



(d) Ca Ka1

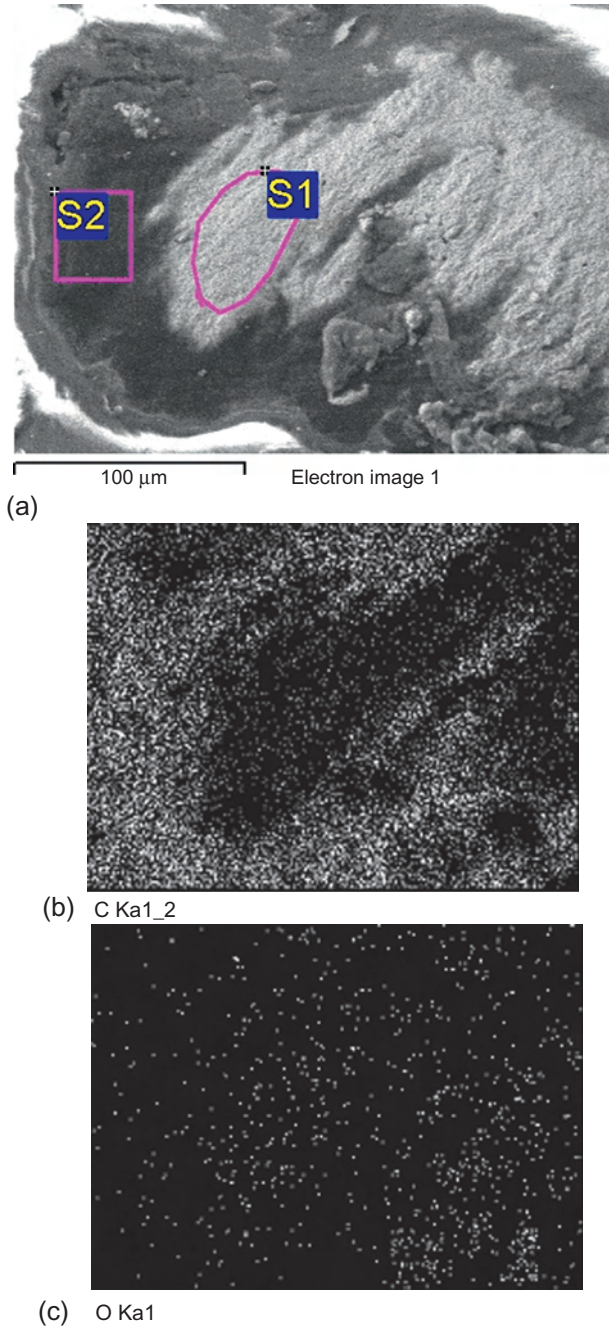


(e) Ni Ka1

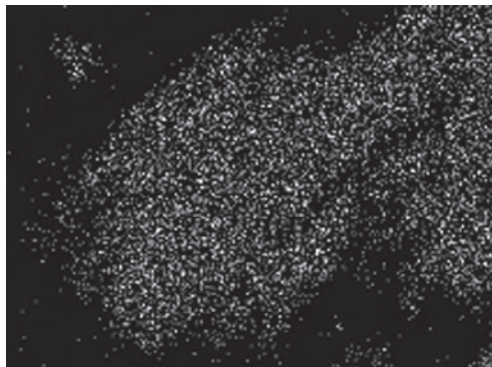


(f) O Ka1

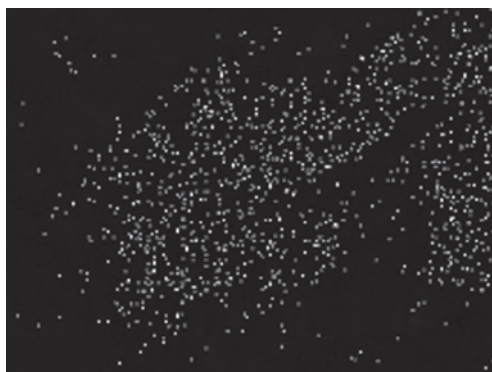
**Figure 26.21** Continued.



**Figure 26.22** Microstructure of the accreted nitinol magnification:  $1220\times$ , acceleration potential (kV): 15.00. (b-e) Elemental structure.



(d) Ti Ka1



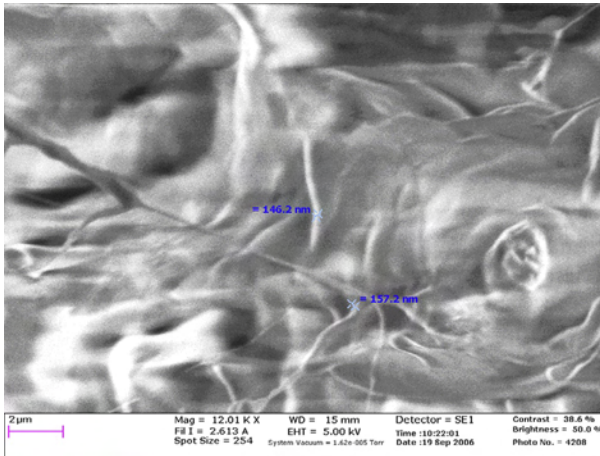
(e) Ni Ka1

Figure 26.22 Continued.

Table 26.3 EDX-analysis of the place shown in Figure 26.22a

Spectrum	C	O	Ti	Ni	Total
S1	49.44	13.27	26.05	11.23	100.0
S2	98.93		1.07		100.0
Max.	98.93	13.27	26.05	11.23	
Min.	49.44	13.27	1.07	11.23	

internal space around the spongiform osteal tissue defect had connecting tissue in the form of trabeculae and lacunae, which were filled in by osteal brain and spongy material. From the medullar spaces of an osteal bed, trabeculae could be seen, consisting of reticulofibrous osteal tissue. The osteal beams were wide with considerable quantities of osteocytes densely packed together and surrounded by thick rows of osteoblasts. Around the trabeculae, considerable quantities of osteoblasts were observed.



**Figure 26.23** The organotypical structures near to the titanium implant.

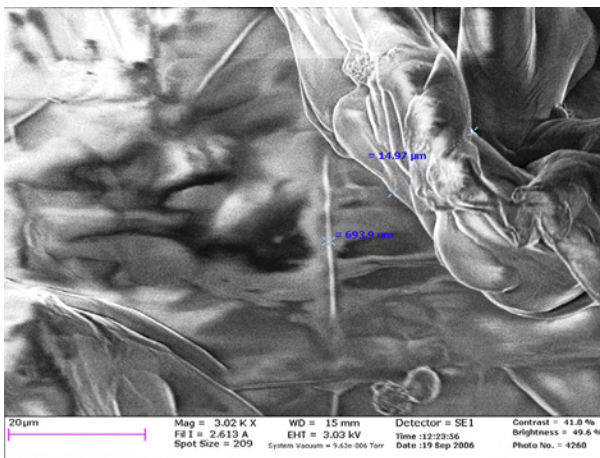


**Figure 26.24** The organotypical structures near to the nickel-titanium implant.

The development of connective tissue (Figures 26.23 and 26.24) in the implantation zone confirmed that the process of osseointegration had occurred. Measurements showed that if near an NiTi implant their characteristic dimensions ranged from 700 nm up to 15 mm (Figure 26.23), whereas around porous Ti more shallow bonds of about 150 nm were formed.

Due to their low durability, nitinol implants can only be recommended for use as plastics for soft and hard tissues defects. Another interesting aspect of developing this branch of implantology is the possibility for CAD-supported creation of objects with controllable porosity. These have better reconciliation of parameters (modulus of elasticity, Poisson's ratio, coefficient of thermal expansion, etc.) between bone tissue and implant material.

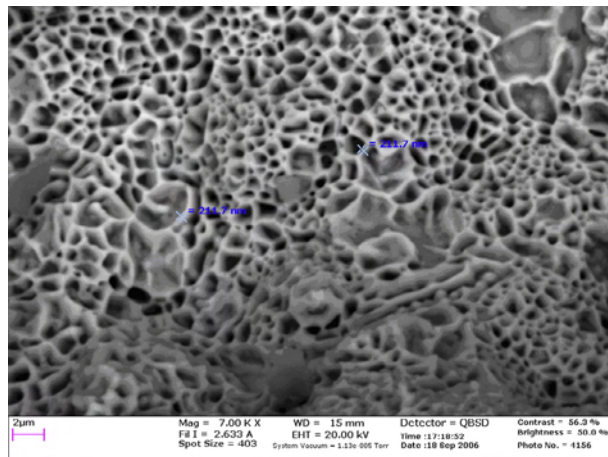


**Figure 26.25** SHS+SLS-synthesized nitinol surface with a developed nano fractal structure.

Highly magnified SEM imaging of the implant surface was used to thoroughly examine the effect that the surface morphology and implant porosity had on the biomechanical integration of the implant with the surrounding bone tissue (see [Chapter 11](#) and [2]). [Figure 26.25](#) shows a close up of [Figure 2](#) from [Chapter 11](#), which shows the sintered nitinol surface ([Figure 26.22](#) shows the surface at lower magnification) at a magnification of 7.000 KX. It was found that the synthesized nitinol surface had a developed nano fractal structure. The nanostructures had a low dimensional self-organization. The wall size of the synthesized nanostructures ranges from about 140 to 460 nm, while the structure itself is about 2-5  $\mu\text{m}$ . It is therefore possible that the developed micro- and nanostructured nitinol surface promotes biointegration.

Histological analysis showed that there was active biointegration of the porous implants with the bones of the animals under consideration. The NiTi implants showed no adverse tissue reactions and there was no evidence of either localized or general corrosion of the bone surface. The implants were assessed according to their biocompatibility, bone contact, and ingrowth. The bone histology and microhardness parameters showed that the bone behavior in contact with the implants was similar to that of the surrounding cranial bone. The SLS-made porous nitinol therefore appears to be a suitable material for craniofacial applications.

## 26.4 Finite-elemental optimization of SLS-obtained implants' porous structure

Intraosseous dental implants are effective for dentition correction. The development of dental implantation depends on achieving osteointegration by improving the intraosseous parts of the implants. Implants with the open type of porosity can manage the load if used as one-root teeth substitutes, but break under the load of the first molars.

Therefore studies of the stress-strain behavior of porous implants under the masticatory load or pressure are needed. The structural and strength properties of the porous implant are also important. The finite element approach (*ANSYS*) is used for solving related problems [39].

One way of approaching implant synthesis is the process of an SLS allowing the manufacture of dental implants with open porosity. Earlier we showed the possibility of the layer-by-layer laser synthesis of titanium and nitinol scaffolds with complex porosity architecture and controllable permeability and particle size, in order to confirm their suitability for tissue engineering.

We now turn to the use of *ANSYS* bundled software to study the SLS-obtained porous implants' mode of deformation. *ANSYS* is already widespread among development-engineers because it can solve the most complex problems of deformable body mechanics and it is adaptable for different end-consumers. Further, it can be used in constructional stomatology.

The different studies in this area are listed below (see references in Ref. [40]):

- “Removable prosthesis—implant—bone” numerical modelling. Variable parameters of size and density of the bone allow the study of the biomechanical foundations of the interaction between the osseous structures of the lower jaw and the full removable prostheses, of a different construction, with the intraosseous implants fixing them.
- Research into the peculiarities of tooth and periodont when in a deflected mode under the dynamic load and into the protective role of the snag. This is carried out by using the finite-elemental model of the teeth-jaw segment of the central maxillar incisor area.
- Investigation of the stress distribution in hard tooth crown tissues with different scopes for defect as well as in the inserts under exposure to physiological loads.
- Comparative analysis of the results of modelling the deflected mode of different pivot crown constructions mathematically.
- Finite-elemental analysis of deflected mode with cavities replaced, in a medial-occlusive way, by the distal insertion of ceramic material or by the plug of a photocurable composite.

However, the exact interaction between the porous structure of the implant and the bone tissue is still unclear.

It is important to know how porosity size influences the interaction between the tissue and the bone. For both particle shapes, the implant is synthesized by the SLS method. Their spatial orientation contributes to the deflected mode of the system. The objective of the analysis was to calculate how to optimize the structure of the implant. The analysis allows one to establish a system to form the prosthesis, which will be both porous enough and meet the masticating pressures of the other. A bone-implant interaction model is needed to carry out the calculations.

It was proposed the changes of the stress at the contact zone should be observed while changing the porosity size. Further, the influence of the internal structure (the particle size) and the shape of the implant upon the originating stresses, resultant deflections, and unit strains are of interest.

A simplified implant model of cylindrical shape (Figure 26.27a) was used for the numerical simulations. Its diameter was 8 mm and length was 14 mm. This construction was placed in the cavity of the spongy bone tissue. To shorten the simulation process,

the model volume was quartered by symmetrically scaled meshing. However, the boundary conditions were imposed on the symmetrical model faces (Figure 26.27c).

As the SLS-obtained implants have a porous structure, the pictorial representation of the model was changed. The implant porosity was determined by the structure of the ordering objects (that is, the particles of the sintered powder) with regular shape (balls or cylinders were used) (Figure 26.26).

The porosity value was adjusted for the change in ball diameter (Figure 26.26a-c). This value was also expressed by changing how much the ball overlapped with its diameter, evaluated in percent. The relative configuration of the objects didn't vary through the study. For the balls, only density packing was appropriate, and every following layer was placed in the holes formed by the previous one.

The material was designed as follows:

1. One object (for example, the ball) is created.
2. This object was copied several times (four times for this study) along the  $X$ -axis of the distance defining the porosity. (This could be 98% or 95% of the ball diameter, so that overlapping was of 2% or 5%, respectively.)
3. The duplicated process is along the  $Y$  (4 times) and the  $Z$  (10 times) directions also. In these cases, it was necessary to calculate that objects fell into the holes of the close-packed structure.

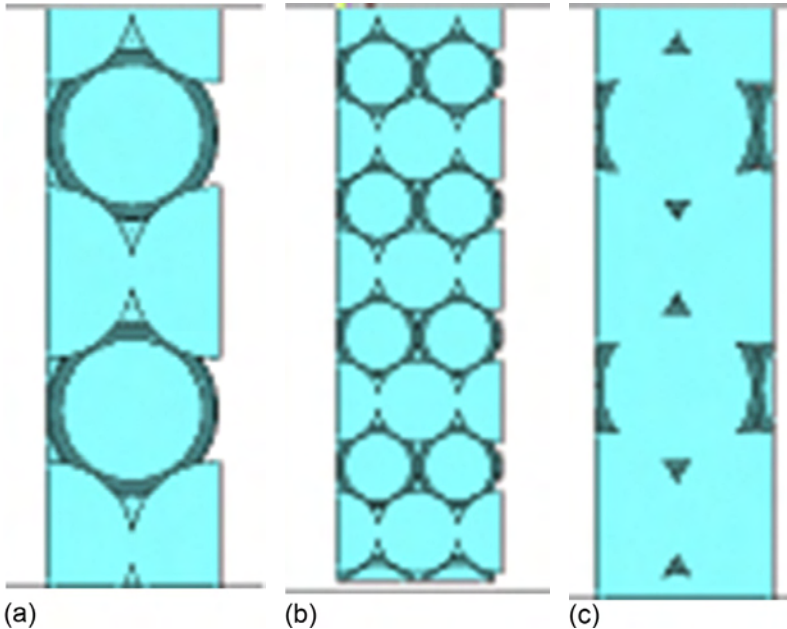


**Figure 26.26** Changing of the calculation model porosity: (a) ball  $d = 2$  mm, overlapping of 2% from  $d$ ; (b) ball  $d = 1$  mm, overlapping of 2% from  $d$ ; and (c) ball  $d = 2$  mm, overlapping of 9% from  $d$ .

Using the built in *ANSYS* function (VINV), a cut-and-paste model was produced. This was done either by a volumetrical cylinder modelled using this program or by another figure built in a different CAD-system. The dowel model was built in the *Solid Works* program and then imported to *ANSYS* as a \*.sat file (Figure 26.27). At this stage, the problem is the appearance of improper surfaces, volumes, and small lines when the intersection of complex-shaped volumes is being built. This causes difficulties in building. Hence, volume size was measured by SCAL throughout the building process. The volume obtained by cutting should be restored to its original size. A process of fragmentation of a construction with a coarse grid of finite elements to optimize the time of the calculations is often not available after such operations. Though a finer grid gives a more accurate result, the time it takes for the calculations becomes unacceptable. Therefore, it was necessary to reject some intermediate constructions (for example, 7% overlapping for 2 mm ball's diameters).

The spongy bone (Figure 26.27b) formed the surrounding volume, remotely attached at a distance of 6 cm. The cylindrical or complex dowels were 1.5 cm × 2 cm. The study used 20-node SOLID95 element to assess the structure of the titanium. It allowed for modelling of the transitional tasks and stress-strain behavior, as well as importing of the model from the CAD system. However, this element is not suitable for materials with shape-memory capabilities because hyperelasticity was not among the special properties of *ANSYS*.

Nitinol is defined as a hyperelastic material as it has an elastic potential energy (or function of the deformation energy density), which is a scalar function of one deformation or strain tensor. Its existent stress component is determined by a derivative of a component of strain. It can be exposed to heavy deformations and displacements without sizeable volume changes occurring. For materials of this kind, the theory of heavy deformations should be applied. Thus, for nitinol, the SOLID187 3-D-element with 10 nodes was used. In the interaction (contact) zone between the implant and bone tissue, the mesh of FE was concentrated. The boundary of the contact was described via TARGE170 and CONTA174 contact elements. The TARGE170 element was generated on the implant surface while the CONTA174 element was used on the internal surface of the bone cavity. We considered a yielding-yielding contact that implies a deformation of both materials.

For the sake of this experiment, it was important to calculate the stresses at the contact zone and in the bone tissue and porous metal part of the model. A comparative analysis of the behaviors of the two types of titanium alloys was undertaken. For titanium, the Young modulus was  $E_X = 1.1025 \times 10^{11}$  Pa and Poisson ratio  $\nu_{XY} = 0.32$ , while for nitinol (NiTi-phase)  $E_X = 48 \times 10^9$  Pa and  $\nu_{XY} = 0.33$ . The spongy tissue parameters were  $E_X = 6.89 \times 10^9$  Pa,  $\nu_{XY} = 0.33$ .

The following boundary conditions were applied to the construction being modelled (Figure 26.27c). The chewing load experienced by teeth is 240 N [1]. Taking the size of the implant into consideration, the pressure applied to the top external surface of implant was set at 1.19 MPa. As mentioned above, the same conditions were set for the construction's cut. The bottom of the bone surface was fastened so that it was prevented from displacing relative to the Z-axis or to the X-Y axes, at the front.

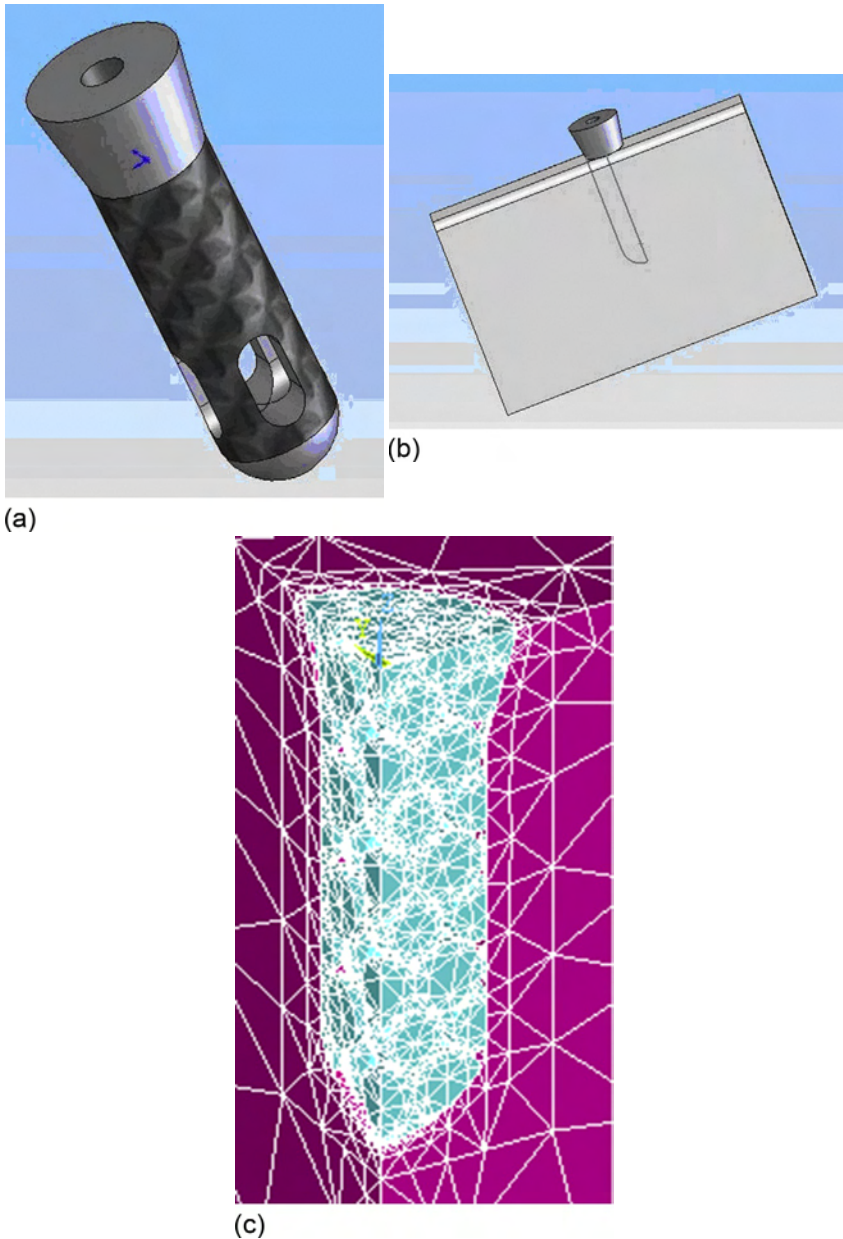


**Figure 26.27** Modelling the implant by *SolidWorks* (a), the implant inserted in the bone tissue (b), and *ANSYS* meshing (c).

The solution was produced in two steps with the *ANSYS* solver. First, the implant “penetration” was achieved in the contact area of the spongy bone. This is achieved by the displacement of the top surface layer along the *Z*-axis. The solution did not disturb this and the loading from the first step was kept. In the second step of the solver, the chewing load was put into force. In the case of the nitinol implant, the “Large Displacement Static” solver was used during the first step of loading because of the “shape-memory effect” characteristic of this material.

Originally, a cylinder-shaped implant of the same size was used to adjust the model. During the first stage of simulation we changed the powder size from 2 to 4 mm. This shortens the calculation time. The diameter overlapping was also increased from 2% to 9%. For the purposes of comparison, we studied two materials, titanium and nitinol. At the second stage of comparison, the model structure was in the cylindrical form of particles. Here we changed the structure of the porosity as a percentage of the cylinder overlapping by height from 2% to 4%. At the third stage of modeling, we studied the influence that the common implant shape had when introduced into the spongy bone construction. The shape of the prosthesis (cylinder or dowel, [Figure 26.27](#)) and its porous internal structure were designed at this stage. Finally, the dependency of the simulation results on the loading direction was shown, that is, how the results of the simulation changed under both normal and tangential deformation, compared to their absolute values, applied to the upper implant surface.

The results of the stress and displacement simulation show that when the overlap of the small particles that constitute the implant (“balls” or “cylinders”) increases, strains and displacements in titanium increase, while stresses drop. For the nitinol structure, when overlapping was increased (in a material approaching a cast one rather than a porous one) stresses, strains, and displacements decreased. Judging by the absolute value, the stress-displacement parameters for titanium are lower than those of the nitinol. Variation of the particle size from 2 to 4 mm shifts the tendencies insignificantly.

The influence of the internal and external shape of the implant upon the strains, stresses, and displacements is complex. First, the implant of a complex shape has higher values of strains, stresses, and displacements than one with a simple cylindrical shape. The shape of the powder particles also influenced the stress-strain behavior: cylinder-shaped particles had higher values of displacements but lower ones of stresses and strains. Generally, the behavior of the nitinol structure is preferable to that of the titanium structure.

Looking at the stress diagram in the graphics mode, we can observe the environmental stress in the implant-bone system in the contact zone, but also in the place of connection between the objects constituting the model. The diagrams are presented in [Figure 26.28](#) for comparison. The cast implant provided the normal loads as well as the tangential ones. The cylinder-shaped implant was a heavy load upon the surface and likely to damage it. The porous dowel of the complex shape tended to release its loads into the space around it and relieve the bottom of the dental alveolus from it. This transforms a part of the implant-bone load into the internal load of the prosthesis. The internal loads can then fasten to the deterioration of the implant. But, because the implant is porous, the tissue will grow into the pores and increase the reliability of osteointegration. Though this was not taken into consideration while making the calculations, it can still be studied afterwards.

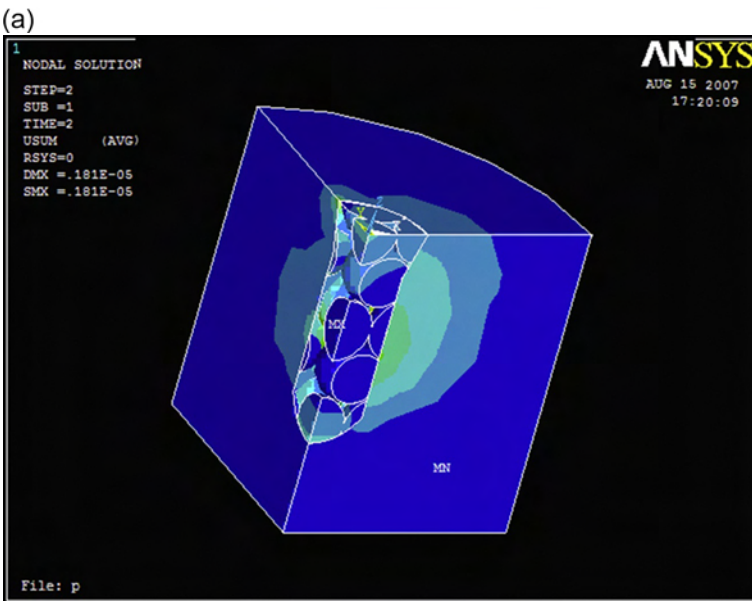
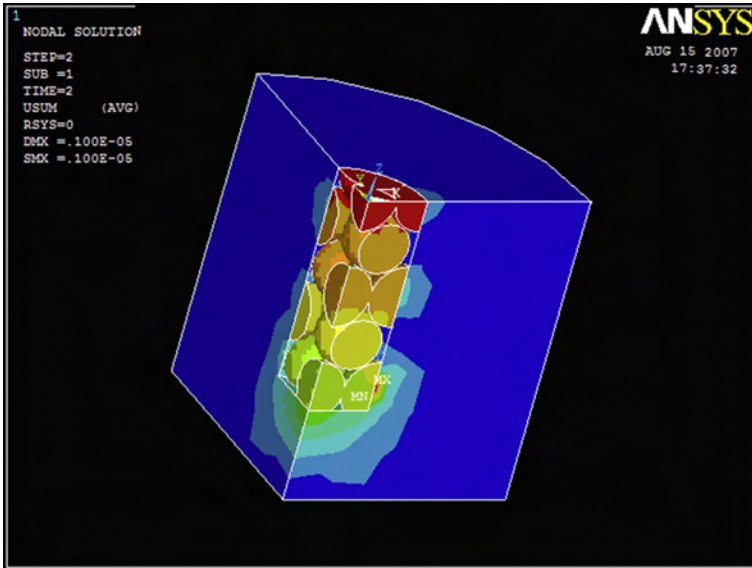
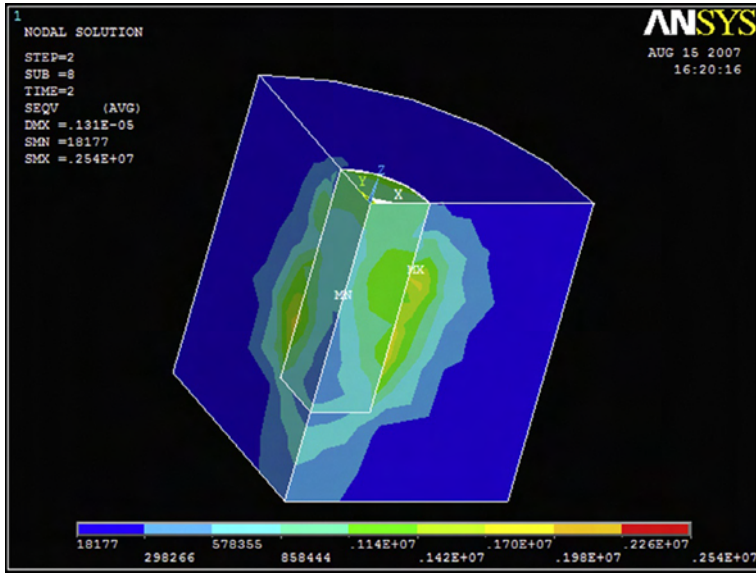


**Figure 26.28** Assumption diagram for stresses and strains in the cylinder-shaped (a), in the complex-shaped [Figure 26.27a](#) (b) and cast (c) implant in the bone tissue.



(C)

Figure 26.28 Continued.

Research has shown that a rough or porous implant surface ensures that there is substantial contact between the bone tissue and the prosthetic device. This results in a more efficient, stronger biomechanical relationship between the implant and the bone. It is also desirable that the contact surface topography corresponds to the bone structure.

The SLS technique allows for picking the right approach to form the prosthesis with a certain structure and, at the same time, regulates its surface roughness and porosity. These characteristics can be controlled to provide a better penetration of the tissues into the implant material.

The study therefore revealed that the absolute values of stresses, strains, and displacements decrease and the implant density increases when the overlapping degree is increased. A comparative simulation has shown that the maximum values of all the investigated parameters observed for the porous nitinol are different for porous Ti. Further, it has shown that bigger displacements and strains occurred with smaller stresses.

## 26.5 The SLS-assisted functional design of porous drug delivery systems based on nitinol

For the last decade, the application of microfabrication methods has led to the development of microelectromechanical systems (MEMS), bio-MEMS, total analysis microsystems, lab-on-a-chip, and other microdevices [41,42]. For instance, the

microfabrication techniques facilitated the creation of novel drug-delivery microdevices and components of microdevices that improve the therapeutic effect of drugs, such as microneedles, micropumps, microvalves and implantable drug delivery systems (DDSs) [43]. Major microfluidic components include:

- sample introduction, loading, and, in some cases, sample preparation
- fluid propulsion, for example reagents, washing or calibration fluids, through micron-sized channels
- valve functioning
- fluid mixing and/or isolation
- small volume sample metering
- sample splitting and washing
- temperature control of the fluids.

A wide range of micro-fluidic products such as pumps, valves, mixers, and flow sensors has been demonstrated [44,45]. The main challenge is how to create miniaturized systems that integrate different microfluidic components to perform certain functions at high speeds throughout.

In general, the fluid propulsion can be put into action mechanically, electrically, or thermally [41,44,45]. Each of these approaches has its own advantages. Here, the thermal methods of propulsion will be discussed. In the case of phase-change pumping, the driving pressure is caused by the volume change due to the phase transformation from one state to another under the temperature variation. Owing to a high heat exchange rate in small channels, this mechanism scales down well to the microdomain. However, thermal methods require careful control of the local temperature. An essential component in the microfluidic system is that the control can stop and start the fluid flow. Different designs use different methods of actuation, such as magnetic, pneumatic, hydraulic, or thermal-electric. The delivery of precisely metered fluids from one reservoir to another in a well-controlled sequence is important for many microfluidic applications. Inkjet print cartridges are one of the most well-known commercial applications of microfluidic devices.

Various microfluidic propulsion technologies have been reviewed and compared with regard to the choice of materials, the maturity of the technology, and the possible volumetric flow rates. Intermetallic NiTi has, even in a porous state, a high specific strength, corrosion resistance, damping characteristics, and a unique shape memory effect (SME) [2,46]. In the case of nitinol, its biocompatibility, physical properties, and the SME observed, even in a porous state, suggests that this material may offer substantial gains in orthopaedic implants and DDS [47–49]. To achieve these gains, implant elements need to be created that can change their shape after implantation. This would be achieved by exploiting the SME of nitinol that can be initiated at the temperature of a living organism. These shape changes have three primary benefits: (1) enhanced bone fixation, (2) minimally invasive surgery, and (3) improved drug saturation. In the field of controlled drug delivery, self-expanding (which occurred here owing to the SME) in *in vivo* devices that use diagnostic measurements to control the drug release will be widely developed in future. Microscale therapeutic and diagnostic systems are fundamental for the development of these self-regulated

(within a close loop) drug delivery devices. They can be implanted inside the body to monitor concentrations of specific target drugs and deliver therapeutic agents if necessary.

RP technology has great potential for engineering implants, scaffolds, and DDS with a pre-specified and reproducible external and internal surface morphology useful for bioengineering applications [5,9,29,38,43,50]. The SLS method is able to rapidly synthesize reproducible, highly complex three-dimensional data ( $\mu$ CT or MRS) for each patient, and internal structural features as well. Another application for the porous structures is in membrane technologies [2] and in the creation of dosing devices for the pharmaceutical (medical) industry. Studies have suggested [9] synthesizing a porous polymeric DDS implant with a bioactive preparation by the method of SLS. The implant dissolves after a time in the patient.

In earlier studies, it was shown that the SLS process typically produces materials with high values of corrosion resistance and porosity, significant water absorption ability, and a well-developed surface structure [2,20]. A controllable internal structure of the interconnected porous channels provides a framework for the bone that ensures it grows into the matrix of the material, thus increasing the interfacial area between the implant and the tissue, and thereby reducing the shift of the implant in the tissue. Also, some suitable channels could be available for drug release into the blood, aimed at reaching the connective ingrown tissue, thereby preventing necrosis of the penetrated cells. The present report is dedicated to the functional design of porous DDSs based on laser-assisted-manufactured nitinol.

The possibility for monitoring and control of the drug release within a spatial and temporary scale is a key requirement for therapeutic use of 3-D porous matrices for storage and medical feeding. To achieve this, it has been suggested that we create porous matrices out of nitinol with encapsulated drugs and/or nanoparticles. Depending on the type of 3-D matrices (CAD structure, as in Figure 26.14a) the penetration speed can be controlled. Since the synthesized 3-D nitinol matrices possess the SME, the drug release velocity should be regulated by changing the pore sizes in the nitinol when under the austenite-martensite phase transformation.

During the heating stage, in which body temperature rises (curves (a), (b), and (d) in Figure 26.29), the load of the stress condition in the NiTi occurs, the pore sizes decrease, and the biological solution is “extruded” from the pores (Figure 26.30a). During the cooling stage, in which the body temperature reverts to its normal state (i.e., “a patient is recovered,” curves (d), (c), and (a) in Figure 26.29), the drug solution intake stops (Figure 26.30b).

Shishkovsky *et al.* [46] have shown that in the presence of porosity, a change of the NiTi stoichiometric composition (even by a few percent) or the addition of alloying elements (Fe, Mo, etc.) can all shift the interval of the back and forward reactions of the austenite-martensite transformations with regard to higher and lower temperatures (compared with cast NiTi). Besides, in the study [46], the method of measuring the dependence of specific resistance upon temperature revealed that changes in SLS and SHS processing influenced the temperature range of SPE in NiTi. Determining all the parameters can therefore lead to the therapeutic effect of delivering the drugs through SPE.

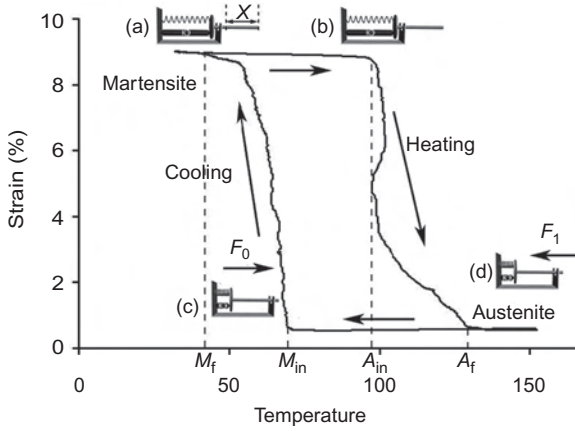


**Figure 26.29** The main steps of the DDS functioning based on the SME. See text for explanation.

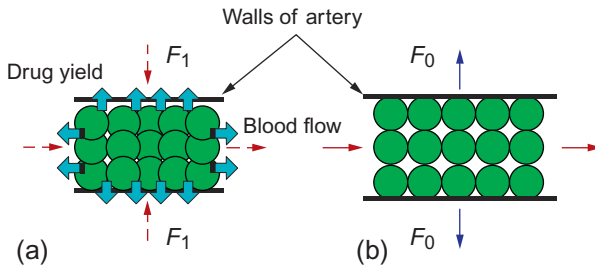


**Figure 26.30** (a, b) The porous 3-D NiTi scaffold behavior during the blood vessels flow.

A general model can be created of the functioning of DDS based on SPE in a porous biocompatible nitinol matrix obtained by SLS, in turn based on individual tomography data. The SME temperature range shift is facilitated by changing the conditions of the SLS and/or the composition and porosity of the sample.

Deformation and stress produced in NiTi creates a useful displacement and produces a force necessary to cause drug release from the pores. The basic stages of the DDS functioning are connected with a complete or incomplete martensite transformation at the body temperature level. We suggest after theoretical modelling and numerical simulations [51] that microdevices of this type can be used repeatedly.

## 26.6 Future remarks

Humans’ average lifespan continues to increase. As a result, there is a significant and growing portion of the population, evident from clinical medical practice, that is experiencing serious problems associated with old age, including organ, tissue, bone, and joint degradation. Advances in orthopedics have helped to enhance quality of life

for many individuals; however, there is still further room for improvement. Future progress in orthopedics will rely on the development of novel biocompatible materials and new ways of producing implants and tissue engineering scaffolds with improved functionality of materials. In order to address this problem, we have studied a combination of novel biocompatible materials and advanced laser-assisted manufacturing technology to produce orthopedic implants that will exceed the functionality and benefits of current implant technologies.

Orthopedic implants must be designed to act as substitutes for human tissues. Hence, the implants should combine, along with other parameters, characteristics like biocompatibility, durability, and physical properties that match the underlying tissue, simplicity of manufacturing, and geometrical accuracy. As mentioned above, several studies have shown that the application of a rough (uneven) or porous surface at the bone/implant interface makes adhesion between bone tissue and implant/scaffold substantially higher. This results in a more effective, stronger biomechanical connection between implant and bone.

The topography of the contact surface should also match bone structure. Bone shape and size in the human body differ from person to person. It is therefore difficult to achieve a durable, solid connection when relying only upon biological fixation with noncustomized geometries. Hence, development of a method that allows for alternative types of fixation to the bone surface that can be adapted for individual structural peculiarities would be highly advantageous.

A conventional material used for implantation is pure titanium. It has high biocompatibility and corrosion resistance in comparison with steel and other materials. Alloys based on Ti-6Al-4V are also widely used. Our research suggests that nickel titanium (NiTi, intermetallic phase) is a suitable material due its properties, even in a porous state, of high specific strength, of corrosion resistance, its damping characteristics, and its unique SME that is the result of thermoelastic martensite transformations within the material.

The biocompatibility of nitinol, its physical properties, and the SME peculiar to it, even in a porous state, suggests that there might be substantial gains in orthopedic implants from using this material. These gains center on creating implant elements that change shape after implantation due to the SME being initiated at the temperature of a living organism. These shape changes have primary beneficial effects: (1) enhanced bone fixation, (2) minimally invasive surgeries, and (3) improved drug delivery. Understanding the effect that varying manufacturing process parameters and material powder composition has on nitinol structures and their physical and mechanical characteristics, including thermally induced shape changes, stiffness, and porosity, allows us to design the optimum implants.

With the use of advanced manufacturing methodologies combined with medical imaging, it is now possible to scan the geometry of a specific patient, and thus customize the implant for that patient. This can be achieved by using modern CT or MRI devices combined with digitally driven manufacturing processes. Two such manufacturing processes are the SLS/M and the LENS. Both technologies are capable of forming a structure layer-by-layer directly from digital data that represents the geometry of the intended structure.

Developing near-net shape methods of tissue engineering scaffold and implant manufacturing is crucial to the future of laser-additive technology. In the long term, artificial bio-MEMS devices (implants with SME, DDS) will find a substantial market in the medicine and pharmacological industries. Interdisciplinary cooperation in research and development is important in order to achieve breakthroughs and to find new approaches to designing products such as biodegraded scaffolds and implants.

## Acknowledgments

This chapter was completed while the author was at P.N. Lebedev Physics Institute of the Russian Academy of Sciences. All the studies were conducted in the framework of the research grants (N 13-08-97001p Povoljie-a; N 10-08-00208-a; N 07-08-12048-ofi) of the Russian Foundation of Basis Researches and the Grants of Presidium of Russian Academy of Sciences in the framework program, “Fundamental sciences for medicine”—stages 2005-2006 and 2009-2010. The author is grateful to Prof. Morozov Yu.G. for his assistance with SEM, Prof. Volova L.T. with Ass. Fokeev S. for the preclinical trial, and Ph.D. Volchkov S.E. for the biomedical testing with MMSC on proliferation activity and cell aging.

## References

- [1] V.E. Gunter, *Delay Law a New Class of Materials and Implants in Medicine*, STT Publishing, Northampton, MA, 2000.
- [2] I.V. Shishkovsky, *Laser Synthesis of Functional Mesostructures and 3D Parts*, Fizmatlit Publications, Moscow, 2009.
- [3] S. Swann, Integration of MRI and stereolithography to build medical models: a case study, *Rapid Prototyp. J.* 2 (4) (1996) 41–46.
- [4] J.M. Taboas, R.D. Maddox, P.H. Krebsbach, S.J. Hollister, Indirect solid free form fabrication of local and global porous, bio-mimetic and composite 3D polymer-ceramic scaffolds, *Biomaterials* 24 (2003) 181–194.
- [5] K.F. Leong, K.K.S. Phua, C.K. Chua, et al., Fabrication of porous polymeric matrix drug delivery devices using the selective laser sintering technique, *Proc. Inst. Mech. Eng. Part H* 215 (2001) 191–201.
- [6] E. Berry, J.M. Brown, M. Connell, et al., Preliminary experience with medical applications of rapid prototyping by selective laser sintering, *Med. Eng. Phys.* 19 (1) (1997) 90–96.
- [7] K.H. Tan, C.K. Chua, K.F. Leong, et al., Scaffold development using selective laser sintering of polyetheretherketone—hydroxyapatite biocomposite blends, *Biomaterials* 24 (2003) 3115–3123.
- [8] N.K. Vail, L.D. Swain, W.C. Fox, et al., Materials for biomedical applications, *Mater. Des.* 20 (1999) 123–132.
- [9] C.L. Liew, K.F. Leong, C.K. Chua, Z. Du, Dual material rapid prototyping techniques for the development of biomedical devices. Part 1: space creation, *Int. J. Adv. Manuf. Technol.* 18 (2001) 717–723.
- [10] N.K. Tolochko, V.V. Savich, T. Laoui, et al., Dental root implants produced by the combined selective laser sintering/melting of titanium powders, *Proc. Inst. Mech. Eng. Part L* 216 (2002) 267–270.

- [11] R. Jamieson, B. Holmer, A. Ashby, Development of new orthopaedic products, *Rapid Prototyp. J.* 1 (4) (1995) 34–41.
- [12] L.C. Hieu, E. Bohez, J.V. Sloten, et al., Design for medical rapid prototyping of cranio-plasty implants, *Rapid Prototyp. J.* 9 (3) (2003) 175–186.
- [13] S. Gopakumar, RP in medicine: a case study in cranial reconstructive surgery, *Rapid Prototyp. J.* 10 (3) (2004) 207–211.
- [14] Z. Chen, D. Li, B. Lu, et al., Fabrication of artificial bioactive bone using rapid prototyping, *Rapid Prototyp. J.* 10 (5) (2004) 327–333.
- [15] D.M. Gureev, A.L. Petrov, I.V. Shishkovsky, Method of medical implants fabrication from the biocompatible materials, Patent Russian Federation No. 2218242, claim N 99102751/02, 1999, date of priority 11.02.1999.
- [16] V.I. Kalita, Physics and chemistry of bioinert and bioactive implant surface fabrication. Review, *Fiz. Khim. Obrab. Mater.* 5 (2000) 28–45(in Russian).
- [17] A. Gaggl, G. Schultes, W.D. Mukller, H. Karcher, Scanning electron microscopical analysis of laser-treated titanium implant surfaces: a comparative study, *Biomaterials* 21 (2000) 1067–1073.
- [18] S. Hansson, A conical implant-abutment interface at the level of the marginal bone improves the distribution of stresses in the supporting bone, *Clin. Oral Implants Res.* 14 (2003) 286–293.
- [19] O.H. Surov, *Teeth Prosthesis on Implants*, Medicine Publications, Mocsow, 1993.
- [20] I.V. Shishkovskii, I.A. Yadroitsev, I.Y. Smurov, Selective laser sintering/melting of nitinol-hydroxyapatite composite for medical applications, *Powder Metall. Met. Ceram.* 50 (5-6) (2011) 275–283.
- [21] G. Binyamin, B.M. Shafi, C.M. Mery, *Biomaterials: a primer for surgeons*, Semin. *Pediatr. Surg.* 15 (4) (2006) 276–283.
- [22] A.S. Fauci, et al., *Harrison's Principles of Internal Medicine*. seventeenth ed., McGraw-Hill Medical, 2008 <http://dx.doi.org/10.1036/0071466339> American textbook of internal medicine.
- [23] P.E. Murray, C. Garcia Godoy, F. Garcia Godoy, How is the biocompatibility of dental biomaterials evaluated? *Med. Oral Patol. Oral Cir. Bucal* 12 (3) (2007) E258–E266.
- [24] S.E. Volchkov, O.V. Tumina, et al., Comparative characteristics of multipotent mesenchymal stem cells from different sources, *Cell Transplant. Tissue Eng.* 3 (2009) 8–9.
- [25] A. Salamon, E. Toldy, Use of mesenchymal stem cells from adult bone marrow for injured tissue repair, *Orv. Hetil.* 150 (27) (2009) 1259–1265.
- [26] V.S. Nirmalanandhan, G.S. Sittampalam, Stem cells in drug discovery, tissue engineering, and regenerative medicine: emerging opportunities and challenges, *J. Biomol. Screen.* 14 (7) (2009) 755–768.
- [27] J.M. Kanczler, S. Mirmalek-Sani, N.A. Hanley, et al., Biocompatibility and osteogenic potential of human fetal femur-derived cells on surface selective laser sintered scaffolds, *Acta Biomater.* 5 (2009) 2063–2071.
- [28] N. Ogura, M. Kawada, W. Chang, et al., Differentiation of the human mesenchymal stem cells derived from bone marrow and enhancement of cell attachment by fibronectin, *J. Oral Sci.* 46 (4) (2004) 207–213.
- [29] I.V. Shishkovskii, Y.G. Morozov, S.V. Fokeev, et al., Laser synthesis and comparative testing of a three-dimensional porous matrix of titanium and titanium nickelide as a repository for stem cells, *Powder Metall. Met. Ceram.* 50 (9/10) (2012) 606–618.
- [30] O. Zinger, K. Anselme, A. Denzer, et al., Time-dependent morphology and adhesion of osteoblastic cells on titanium model surfaces featuring scale-resolved topography, *Biomaterials* 25 (14) (2004) 2695–2711.

- [31] E. Behraves, et al., Synthetic biodegradable polymers for orthopedic applications, *Clin. Orthop.* 367S (1999) 118–185.
- [32] K.J.L. Burg, et al., Biomaterials development for bone tissue engineering, *Biomaterials* 21 (2000) 2347–2359.
- [33] M.T. Duailibi, et al., Bioengineered teeth from cultured rat tooth bud cells, *J. Dent. Res.* 83 (7) (2004) 523–528.
- [34] A. Smith, Tooth tissue engineering and regeneration, *J. Dent. Res.* 83 (7) (2004) 517.
- [35] C.S. Young, et al., Tissue engineering of complex tooth structures on biodegradable polymer scaffolds, *J. Dent. Res.* 81 (10) (2004) 695–700.
- [36] C.Y. Fong, L.L. Chak, A. Biswas, et al., *Stem Cell Rev.* 7 (2011) 1.
- [37] S.E. Volchkov, I.V. Shishkovsky, I.V. Barikov, Influence of porous three-dimensional implants from nitinol on culture of multipotent mesenchymal stromal cells, *Cell Transplant. Tissue Eng.* 8 (1) (2013) 51–56.
- [38] I.V. Shishkovsky, M.V. Kuznetsov, Y.G. Morozov, Porous titanium and nitinol implants synthesized by SHS/SLS: microstructural and histomorphological analyses of tissue reactions, *Int. J. Self Propag. High Temp. Synth.* 19 (2) (2010) 157–167.
- [39] A.B. Kaplun, et al., ANSYS for Engineers: Handbook, Editorial URSS, Moscow, 2003.
- [40] I.V. Shishkovsky, Stress-strain analysis of porous scaffolds made from titanium alloys synthesized via SLS method, *Appl. Surf. Sci.* 255 (24) (2009) 9902–9905.
- [41] J.Z. Hilt, N.A. Peppas, Microfabricated drug delivery devices, *Int. J. Pharm.* 306 (2005) 15–23.
- [42] F.N. Pirmoradi, J.K. Jackson, H.M. Burt, M.A. Chiao, Magnetically controlled MEMS device for drug delivery: Design, fabrication, and testing, *Lab Chip Miniaturisat. Chem. Biol.* 11 (18) (2011) 3072–3080.
- [43] I.V. Shishkovsky, Functional design of porous drug delivery systems based on laser assisted manufactured nitinol, *MRS Proc.* 1415 (2012) mrsf11-1415-ii03-10.
- [44] J.L. Moore, A. McCuiston, I. Mittendorf, R. Ottway, R.D. Johnson, Behavior of capillary valves in centrifugal microfluidic devices prepared by three-dimensional printing, *Microfluid. Nanofluid.* 10 (4) (2010) 877–888.
- [45] E. Gultepe, D. Nagesha, S. Sridhar, M. Amiji, Nanoporous inorganic membranes or coatings for sustained drug delivery in implantable devices, *Adv. Drug Deliv. Rev.* 62 (2010) 305–315.
- [46] I. Shishkovsky, V. Sherbakoff, I. Yadroitsev, I. Smurov, Particularities of electrical resistivity and phase structure in the 3D porous nitinol after SLS/SLM, *Proc. Inst. Mech. Eng. Part C* 226 (12) (2012) 2982–2989.
- [47] S.-R. Guo, Z.-M. Wang, Y.-Q. Zhang, et al., *In vivo* evaluation of 5-fluorouracil-containing self-expandable nitinol stent in rabbits: efficiency in long-term local drug delivery, *J. Pharm. Sci.* 99 (7) (2010) 3009–3018.
- [48] M.D. Dake, W.G. Van Alstine, Q. Zhou, A.O. Ragheb, Polymer-free paclitaxel-coated silver PTX stents—evaluation of pharmacokinetics and comparative safety in porcine arteries, *J. Vasc. Interv. Radiol.* 22 (2011) 603–610.
- [49] S. Sato, Y. Nakayama, Y. Miura, et al., Development of self-expandable covered stents, *J. Biomed. Mater. Res. Part B Appl. Biomater.* 83 (2) (2007) 345–353.
- [50] C.M. Cheah, K.F. Leong, C.K. Chua, K.H. Low, H.S. Quek, Characterization of microfeatures in selective laser sintered drug delivery devices, *Proc. Inst. Mech. Eng. Part H: J. Eng. Med.* 216 (2002) 369–383.
- [51] I.V. Shishkovsky, Simulation of thermomechanical and electrothermal hysteresis phenomena in porous nickel titanium, *Tech. Phys.* 59 (2) (2014) 297–303.